J. Fluid Mech. (2022), *vol*. 937, A33, doi:10.1017/jfm.2022.119

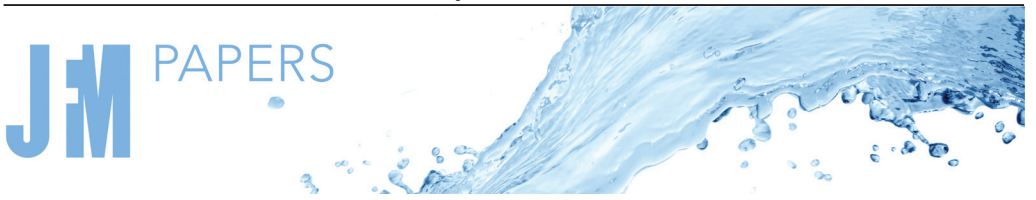

Comparison of the compressible $\mu(I)$ class of models and non-local models with the discrete element method for steady fully developed flow of cohesionless granular materials through a vertical channel

Bhanjan Debnath[1], **V. Kumaran**[1] **and K. Kesava Rao**[1,†]

[1]Department of Chemical Engineering, Indian Institute of Science, Bengaluru 560012, India

(Received 16 April 2021; revised 15 October 2021; accepted 31 January 2022)

The flow of granular materials through a vertical channel is examined using the discrete element method (DEM) and the recent continuum models of Henann & Kamrin (*Proc. Natl Acad. Sci. USA*, vol. 110, 2013, pp. 6730–6735), Barker *et al.* (*Proc. R. Soc. Lond. A*, vol. 473, 2017, p. 20160846), Schaeffer *et al.* (*J. Fluid Mech.*, vol. 874, 2019, pp. 926–951) and Dsouza & Nott (*J. Fluid Mech.*, vol. 888, 2020, p. R3). The channel is bounded by walls separated by a distance $2\,W$ in the x-direction. For the DEM, periodic boundary conditions are used in the z- and y- (vertical) directions with no exit at the bottom of the channel. The governing equations reduce to ordinary differential equations in the x-direction. There is a plug layer near the centre and a shear layer near the wall, as observed in experiments. There is a decrease in the solids fraction ϕ in the shear layer, except for the models of Barker *et al.* and Henann & Kamrin. A modification of the latter gives more realistic ϕ profiles. The thickness of the shear layer depends on $2\,W$ and the bulk solids fraction $\bar{\phi}$. For all the models, solutions could not be obtained for some parameter values. An example is the negative fluidity in the model of Henann & Kamrin. The model of Dsouza & Nott predicts much higher normal stresses, possibly because of large contributions from the non-local terms. None of the models specify a complete set of boundary conditions (b.c.). The DEM results suggest that the slip velocity and the wall friction b.c. lead to a slip length and an angle of wall friction that are independent of $2\,W$. The models are based on extensions of the equations for slow, rate-independent flow. A model that includes collisional effects, such as kinetic theory, should be combined with the present models. A preliminary analysis of the kinetic theory model of

† Email address for correspondence: kesava@iisc.ac.in

Berzi *et al.* (*J. Fluid Mech.*, vol. 885, 2020, p. A27), shows that it may have undesirable feature.

Key words: dry granular material

1. Introduction

The flow of granular materials occurs in a variety of natural and industrial settings such as landslides, desert dunes, silos and rotary kilns. Unlike Newtonian fluids, the mechanics of these flows is not well understood. For several decades, researchers have attempted to develop models based on soil mechanics, metal plasticity, kinetic theory of gases, activated processes, thermodynamics, etc. Owing to the unique dynamical properties in different regimes, such as rate-independent stresses in slow flow and rate-dependent stresses in intermediate and rapid flows, it is challenging to develop a unified constitutive law which predicts the features of all the regimes satisfactorily.

Based on experiments with soils and rocks, Coulomb (1776) (cited in Schofield & Wroth 1968) assumed that the material yields by sliding along rupture surfaces. The shear stress T and the normal stress N acting on the rupture surface are related by the Coulomb yield condition

$$T = \mu N + c, \tag{1.1}$$

where μ and c are constants called the coefficient of friction or the friction coefficient and the cohesion, respectively. Subsequently, other yield conditions were proposed, and models for the kinematics were developed by assuming incompressibility and coaxiality. The latter implies that the principal axes of the stress and the rate of deformation tensors coincide.

The experiments of Reynolds (1885) showed that a dense granular material dilates (reduction in the solids fraction ϕ) when it deforms under shear, and *vice versa*. A modified version of the Coulomb model, known as critical state soil mechanics, incorporates compressibility by modifying the yield condition (Schofield & Wroth 1968; Jackson 1983; Rao & Nott 2008) and specifying a flow rule that relates the stress to the rate of deformation tensor. The flow rule is formulated so that it incorporates rate independence: if all the components of the rate of deformation tensor are scaled by a common factor, the stresses are unaffected.

In a modification of Coulomb's model, an empirical incompressible model was proposed wherein $\mu = \mu(I)$ (Pouliquen & Forterre 2002; GDR-MiDi 2004; Jop, Forterre & Pouliquen 2005). Here, I is called the inertial number, and is proportional to the shear rate and inversely proportional to the square root of the pressure. In the limit $I \to 0$, their relation for $\mu(I)$ tends to a positive constant, thereby recovering the Coulomb model for quasistatic flow of a cohesionless material. The friction coefficient varies monotonically with I, saturating at large values of I. Later, density variation was incorporated by assuming that $\phi = \phi(I)$. This $\mu(I) - \phi(I)$ model will be discussed in detail later.

Goodman & Cowin (1971) introduced an 'equilibrium' stress derived from a free energy function, and a dissipative stress given by the constitutive equation for a Newtonian fluid. The total stress tensor is the sum of the equilibrium stress tensor which depends on the solids fraction and its gradient, and the dissipative stress tensor which depends on

the rate of deformation tensor. Unfortunately, there are many undetermined coefficients. The predictions for inclined chutes and vertical channels involve a length ratio that was speculated to depend on the grain size.

The occurrence of shear bands or zones of intense shearing is another striking feature of granular flow (Nedderman & Laohakul 1980; Pouliquen & Gutfraind 1996; Fenistein & Van Hecke 2003). The inability of the classical plasticity (frictional) model to predict these bands is attributed to the absence of a material length scale in the constitutive equations (Mühlhaus & Vardoulakis 1987). Many models that incorporate a material length scale have been proposed, such as the Cosserat model (Mohan, Nott & Rao 1999; Mohan, Rao & Nott 2002), and various non-local models (Aranson & Tsimring 2001; Pouliquen & Forterre 2009; Kamrin & Koval 2012). Some of these will be discussed later.

The above models deal mainly with slow flow, where enduring contacts between particles is the major mode of momentum transfer. However, the $\mu(I)$ and $\mu(I) - \phi(I)$ models account for inertial effects to a certain extent. In the regime of rapid flow, which is characterized by moderate to low solids fractions and high shear rates, collisions between particles and free flight of particles between collisions becomes important. Many attempts have been made to develop the constitutive equations using extensions of the kinetic theory of dense gases to account for the inelasticity of interparticle collisions and particle roughness (Lun *et al.* 1984; Kumaran 1998; Garzó & Dufty 1999; Kumaran 2006, 2008).

Our study mainly focuses on solving and comparing the compressible $\mu(I)$ class of models (Barker *et al.* 2017; Schaeffer *et al.* 2019) and non-local models (Henann & Kamrin 2013; Dsouza & Nott 2020) with the results of discrete element method (DEM) simulations. A preliminary analysis of a model based on kinetic theory is given in Appendix A. A simple geometry where the shear rate spans the range from slow to rapid flow is helpful in testing models. Examples include plane and cylindrical Couette cells, vertical channels and inclined chutes. The present work is confined to vertical channels of rectangular cross-section (figure 1*a*).

A granular material such as sand or glass beads is fed at the top of the channel and discharges through the exit slot at the bottom. It is assumed that the flow is steady and quantities do not vary in the z-direction (figure 1*a*). Further, it is assumed that the flow is fully developed, so that quantities such as the velocity vary only in the x-direction. The velocity field is given by

$$u_x = 0 = u_z, \quad u_y = u_y(x). \tag{1.2a,b}$$

Such a condition is expected to prevail at locations that are far from the upper free surface and the exit slot. This deceptively simple problem has been examined for several decades (Goodman & Cowin 1971; Savage 1979; Nedderman & Laohakul 1980; Yalamanchili, Gudhe & Rajagopal 1994; Natarajan, Hunt & Taylor 1995; Mohan, Nott & Rao 1997; Wang, Jackson & Sundaresan 1997; Mohan *et al.* 1999; Pouliquen, Forterre & Le Dizes 2001; Ananda, Moka & Nott 2008), but a satisfactory model is lacking.

The DEM is a powerful tool to examine the mechanics of flowing granular materials, and has been used to study many systems such as hoppers (Zhao *et al.* 2018), bunkers (Yu & Saxén 2010), vertical channels (González-Montellano, Ayuga & Ooi 2011), inclined chutes (Bharathraj & Kumaran 2017, 2019) and circulating fluidized beds (Luo *et al.* 2017). Data obtained from DEM simulations can be used to generate density, velocity and stress fields, which form vital benchmarks for comparison with the predictions of continuum models. Unlike the case of simple fluids such as air and water, there

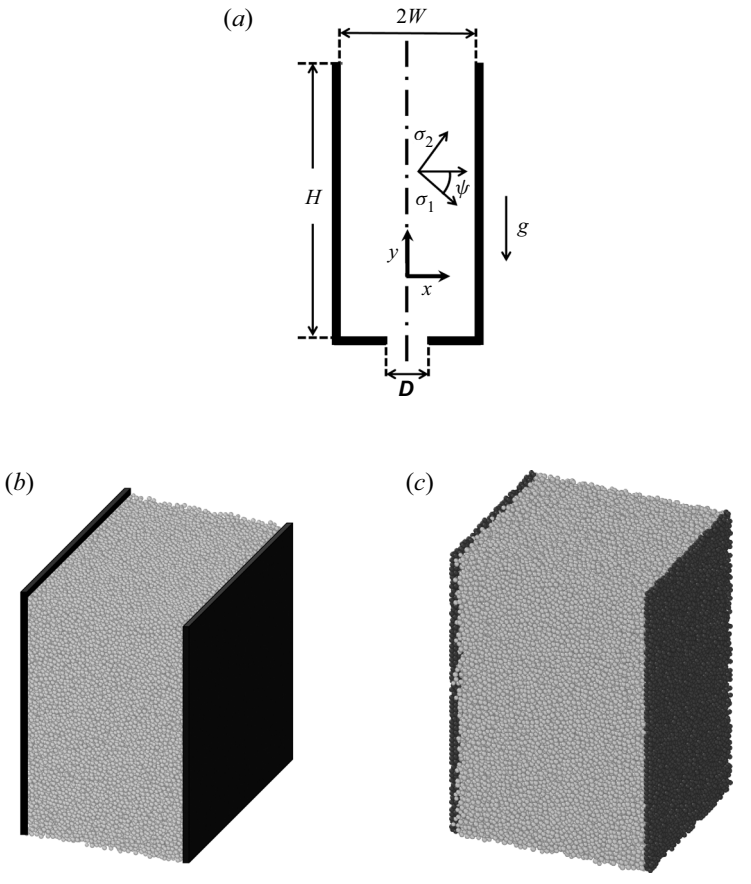

Figure 1. (*a*) A vertical channel with an exit slot. In (*b*,*c*), the exit slot is removed, and the periodic boundary conditions are applied in the *y*- and *z*-directions. The walls are flat and frictional in (*b*), and are roughened by coating them with particles in a dense random packing in (*c*).

is no universally accepted constitutive equation for flowing granular materials. This topic has been examined for several decades, but the end is not in sight. Against this backdrop, it was felt that the proposed comparison of the predictions of continuum models with the results of DEM simulations for flow in a relatively simple geometry may serve to highlight the attractive features and defects of some of the recent models.

2. Details of the DEM

Following Cundall & Strack (1979), the granular material is modelled as a collection of spherical grains that can overlap slightly. Here, we use a linear elastic spring and a viscous dashpot acting in parallel to determine the normal force N_f acting between two particles in contact (Cundall & Strack 1979; Shäfer, Dippel & Wolf 1996). As the material is cohesionless, $N_f = 0$ when there is no overlap between the particles. A similar model is used for the tangential force T_f, but if $|T_f|/N_f > \mu_p$, the coefficient of interparticle friction, $|T_f|$ is replaced by $\mu_p N_f$, with a suitably chosen direction for T_f. Thus the contact

forces are given by

$$N_f = -k_n \delta_n \boldsymbol{n} - m_e \xi_n \boldsymbol{v}_n$$
$$T_f = \begin{cases} -k_t \delta_t \boldsymbol{t} - m_e \xi_t \boldsymbol{v}_t, & \text{if } \dfrac{|T_f|}{N_f} < \mu_p \\ -\mu_p N_f \boldsymbol{t}, & \text{otherwise.} \end{cases} \tag{2.1}$$

In (2.1), $\boldsymbol{n}$ and $\boldsymbol{t}$ denote the normal and tangential directions, respectively, where the former coincides with the direction of the line joining the centres of particles in contact, k_n and ξ_n are the spring constant and the damping constant in the normal direction, respectively, δ_n is the overlap in the normal direction and $\boldsymbol{v}_n$ is the normal component of the velocity at the contact point. For two particles of masses m_1 and m_2 that are in contact, the effective mass m_e is defined by

$$m_e = \frac{m_1 m_2}{m_1 + m_2}. \tag{2.2}$$

This approach is termed the linear spring and dashpot (LSD) model, and has been widely used (Silbert *et al.* 2001; GDR-MiDi 2004; Chialvo, Sun & Sundaresan 2012; Guo & Curtis 2015). However, more sophisticated models for the contact force have also been used. For example, the classical Hertz model (Hertz 1882; Johnson 1987) predicts that $N_f \propto \delta_n^{3/2}$. For tangential loading, the relation between T_f and δ_t is more complicated (Johnson 1987; Vu-Quoc, Zhang & Lesburg 2001). In some cases, results obtained with these models and the LSD model do not differ significantly (Di Renzo & Di Maio 2004; Kruggel-Emden *et al.* 2007). Here, the simple LSD model is chosen as the benchmark for comparison, and computations are done using the open source code LAMMPS (Plimpton 1995).

There are six parameters in the model for the contact forces between particles: the spring constants k_n and k_t, the damping constants ξ_n and ξ_t, the coefficient of interparticle friction μ_p and the coefficient of particle–wall friction μ_w. Following Debnath, Rao & Nott (2017), we choose $k_n = 10^6 \rho_p g d_p^2$, $k_t/k_n = 2/7$, $\xi_n = 180\sqrt{g/d_p}$, $\xi_t/\xi_n = 1/2$ and $\mu_p = \mu_w = 0.5$, where ρ_p and d_p are the density and the diameter of the particle, respectively, and g is the acceleration due to gravity. It is widely acknowledged that k_n should be a few orders of magnitude larger for materials such as aluminium, stainless steel, brass and glass beads (see e.g. Mishra & Murty 2001; Silbert *et al.* 2001; Kruggel-Emden *et al.* 2007), but this would result in a very small time step being used when the equations of motion are integrated. The value chosen is believed to give reasonable results, and reflects a compromise between realistic parameter values and excessive computation time. The time step used is $1.2 \times 10^{-4}\sqrt{d_p/g}$. Debnath *et al.* (2017) estimated the lift on a disc immersed in a rotating bed of granular material, and found that modest changes in the value of k_n by a factor of 10 do not affect the normal stresses exerted on the disc significantly. The value of k_t/k_n is commonly used; it is obtained by considering an elastic collision between a sphere and a flat surface, assuming that the time periods for normal and tangential collisions are equal (Shäfer *et al.* 1996). The chosen values of k_n and ξ_n imply that the coefficient of restitution in the normal direction is 0.7, and the value chosen for μ_p is typical of values for glass beads. The parameters for particle–wall interactions are chosen to be the same as for interparticle interactions.

As is common practice in DEM, we use a slightly polydisperse granular material, with sizes $0.9\,d_p$, $1\,d_p$ and $1.1\,d_p$, and having number fractions 0.3, 0.4 and 0.3, respectively. This is done to prevent the formation of ordered or 'crystalline' layers near the wall.

Some computations were also done for monodisperse materials, and the results did not differ significantly. Only the results for polydisperse materials are presented here. As the lengths are scaled by d_p, velocities by $\sqrt{gd_p}$, time by $\sqrt{d_p/g}$ and forces by $\rho_p g d_p^3$, d_p does not occur explicitly in the scaled equations and hence its actual value need not be specified. Without loss of generality, ρ_p, d_p and g are set to 1 in DEM.

The simulation box is a rectangular parallelepiped, with a bottom and four flat frictional walls, of dimensions $2W$, H and B in the x-, y- and z-directions, respectively (figure 1*a*). Henceforth, such walls will be referred to as 'smooth' walls. The box is filled with particles by uniformly pouring them from the top, and allowing them to settle under the action of gravity. The mass flow rate of the material can be controlled by adjusting the width of the exit slot at the bottom (figure 1*a*). However, for a channel of realistic dimensions, the number of particles N_p that can be handled by the code become excessive. As the flow is expected to be fully developed far above the exit slot, the motion of a reasonable number of particles, say 5×10^4–2×10^5, is simulated by applying periodic boundary conditions in the y- and z-directions. Thus there are no solid walls in the y- and z-directions, and no exit slot (figure 1*b*). Some approaches to incorporating the effect of the exit slot and the walls in the z-direction will be indicated briefly later. If a particle leaves the simulation box with a velocity $\boldsymbol{v}$, it re-enters at the top $y = H$, with the same velocity and the same values of x and z. As noted by Allen & Tildesley (2017), the use of periodic boundary conditions suppresses spatial variations in the y- and z-directions on length scales that are comparable to the dimensions of the box. Results are presented here for $H = 30\,d_p$, $B = 40\,d_p$ and values of $2W$ in the range 30–$80\,d_p$. A few simulations were done with different dimensions, say $H = 30\,d_p$ and $B = 20\,d_p$, and the results did not vary with H and B. The flow properties vary with x-direction, as discussed in § 4. An empty head space volume (with rectangular cross-section of dimensions $2W \times B$, similar to that of the channel) is added at the top, and its height ΔH is adjusted such that a specified bulk solids fraction $\bar{\phi}$ is attained during flow. Here, $\bar{\phi}$ is defined as the ratio of the total volume of the material to the volume of the channel. For N_p particles in the simulation box, the total volume of the particles is $\sum_i^{N_p} (\pi/6) d_{p_i}^3$ and $2W \times B \times (H + \Delta H)$ is the volume of the simulation box. Some simulations are also done for the case of rough walls, where the walls are coated with a layer of stationary particles of diameter d_p (figure 1*c*). The dimension $2W$ excludes the wall particles.

A preliminary study of Debnath, Kumaran & Rao (2019) for flat frictional walls shows that there is no flow for $\bar{\phi} > 0.62$. Steady flow occurs for $0.62 \geqslant \bar{\phi} \geqslant \bar{\phi}_{cr}$ and an oscillatory flow for $\bar{\phi}_{cr} > \bar{\phi} \geqslant \bar{\phi}_m$. Free fall under gravity occurs for $\bar{\phi} < \bar{\phi}_m$. Here, $\bar{\phi}_{cr}$ and $\bar{\phi}_m$ are parameters that depend on $2W/d_p$. The present work is confined to steady flow. A study on the transition to oscillatory flow and free fall will be discussed in a future work.

The simulation box is divided into bins of thickness $1\,d_p$ in x-direction spanning over $(H + \Delta H)$ and B. The velocity and stresses in a bin are calculated by averaging the properties of particles whose centres are in that bin. The solids fraction ϕ is calculated as the ratio of the total volume of the material in a bin to the volume of the bin. The values of the properties are assigned to the centres of the bins. After 2×10^7 time steps, when a steady and fully developed state is attained, the DEM results are time averaged over 5×10^5 time steps. Except at the wall, the maximum distance D_p between the centres of the particles in a bin is $1\,d_p$. For the bin adjacent to the wall, if the bin width is $1\,d_p$, D_p is $(1/2)\,d_p$. To avoid this problem, the width of the bin adjacent to the wall is chosen as $1.5\,d_p$. The standard deviation is very small compared with the sizes of the symbols representing the DEM results, and hence the error bars are not shown.

3. Continuum models

The classical frictional model for plane flow predicts a flat velocity profile, i.e. plug flow, with an indeterminate value for the velocity (Mohan *et al.* 1997). This is at variance with both experimental observations (Nedderman & Laohakul 1980; Natarajan *et al.* 1995; Pouliquen & Gutfraind 1996; GDR-MiDi 2004; Ananda *et al.* 2008) and the DEM results to be discussed in this paper. These show shear layers near the channel walls and a plug layer near the centreline, and a lower value of the solids fraction ϕ in the shear layer.

The model based on the kinetic theory of Lun *et al.* (1984) predicts results in good agreement with the measured velocity profiles when the centreline velocities are matched (Mohan *et al.* 1997), but $\phi \approx \phi_{drp}$ in the plug layer, where the subscript *drp* denotes dense random packing. Hence the underlying assumptions of kinetic theory, such as instantaneous collisions and molecular chaos, are likely to break down in this region. The frictional-kinetic model overcomes this defect by including frictional effects in the plug layer. However, the thickness of the shear layer is much less than that observed (Mohan *et al.* 1997).

An alternative approach is provided by the Cosserat plasticity model of Mohan *et al.* (1999), wherein the symmetry of the stress tensor is relaxed and a balance for the couple stress is solved along with the other balances. The scaled velocity profile (velocity scaled by the centreline velocity) agrees fairly well with data. Thus this model appears to provide an elegant solution, but suffers from the defect that the profile of ϕ is flat. Similarly, Pouliquen & Gutfraind (1996) developed a model based on stress fluctuations that fitted their data for the velocity profiles well, but ϕ was assumed to be constant. The qualitative observations of Natarajan *et al.* (1995) and experiments on two-dimensional flows comprised of circular cylindrical rods (Pouliquen & Gutfraind 1996) suggest that the solids fraction ϕ is lower in the shear layer than near the centre.

Pouliquen (1999) studied the flow of glass beads down an inclined chute with a rough base. He proposed a relation between the stress ratio μ (the ratio of the shear stress to the normal stress), the mean velocity u and the thickness h of the flowing layer. Note that μ is a constant across the layer in this geometry. This relation is valid only for $h > h_{stop}$, where h_{stop} is a critical thickness below which the flow stops abruptly. Pouliquen & Forterre (2002) examined the spreading of an initially hemispherical mass of glass beads down an inclined chute. The friction law of Pouliquen (1999) was used, with some modifications for small values of h to numerically solve depth-averaged equations. The predicted shape of the heap as a function of position and time matched their data well, except when the base had a static layer of material initially. Forterre & Pouliquen (2003) used both glass beads and sand, and fitted their data to the friction law

$$\frac{u}{\sqrt{gh}} = -\gamma_1 + \gamma_2 \frac{h}{h_{stop}(\theta)}, \tag{3.1}$$

where γ_1 and γ_2 are constants, g is the acceleration due to gravity and θ is the inclination of the chute to the horizontal. In particular, $\gamma_1 = 0$ for glass beads, but not for sand.

The group GDR-MiDi (2004) collated data and the results of DEM simulations from various geometries such as plane shear between horizontal plates in the absence of gravity, cylindrical Couette, inclined chute, vertical channel and rotating drum and from various papers. They found it helpful to introduce the inertial number I, defined by

$$I = \frac{|S|\, d_p}{\sqrt{N/\rho_p}}, \tag{3.2}$$

where S is a suitable shear rate, N is a suitable normal stress and d_p and ρ_p are the particle diameter and the particle density, respectively. The inertial number (or more precisely the square of I) is a rough measure of the ratio of the collisional stress to the total stress. Let T denote a suitable shear stress. GDR-MiDi (2004) found that plane shear could be modelled by the relation

$$\mu = \mu(I), \tag{3.3}$$

where the friction coefficient or stress ratio is defined by

$$\mu \equiv \frac{|T|}{N}. \tag{3.4}$$

Equation (3.3) holds provided I is not too large. However, for inclined chutes, (3.3) was valid only for glass beads, but not for sand. This result follows from (3.1), with a non-zero value for γ_1. For rotating drums and heaps, the velocity profiles were not consistent with (3.3). Jop, Forterre & Pouliquen (2005) specified an explicit form for (3.3), and used it in their work (Jop, Forterre & Pouliquen 2006) to solve the incompressible three-dimensional equations for flow down an inclined chute with rough sidewalls. For glass beads, good agreement was obtained between data and model predictions for the profile of the velocity at the free surface of the flowing layer.

Simulations reported in GDR-MiDi (2004) and Da Cruz *et al.* (2005) show that

$$\phi = \phi(I), \tag{3.5}$$

where ϕ is the solids fraction.

Another defect of (3.3) must be noted. Consider plane shear between horizontal plates, in the presence of gravity. If the upper plate is moved and the lower plate is stationary, this model predicts a shear layer near the moving plate, and a static bed of material near the lower plate. Pouliquen *et al.* (2006) state that the thickness of the shear layer tends to zero in the limit of quasistatic flows ($I \to 0$), whereas simulations show that it is of the order of 5–10 d_p.

For plane flow, it has been shown that the incompressible $\mu(I)$ model of Jop, Forterre & Pouliquen (2006) is linearly ill posed for small and large values of I (Barker *et al.* 2015). Here, 'ill posed' means that perturbations to the linearized unsteady equations grow at an unbounded rate as the wavelength of the perturbation tends to zero. By modifying the functional form of $\mu(I)$, Barker & Gray (2017) showed that the model is linearly well posed for $I < I_{max}$, where I_{max} is a constant. Goddard & Lee (2017) showed that the use of a higher gradient model (involving the fourth-order spatial derivatives of the velocity vector in the momentum balance) stabilizes the incompressible $\mu(I)$ model. We note in passing that the classical frictional model is ill posed for both incompressible flow (Schaeffer 1987) and compressible flow (Pitman & Schaeffer 1987).

Consider the $\mu(I) - \phi(I)$ class of models next. It has been shown (Heyman *et al.* 2017) that these are also ill posed for some flow conditions, but can be regularized by adding a term involving a quantity analogous to the bulk viscosity in the expression for the stress tensor. Let $\boldsymbol{\sigma}$ denote the stress tensor, defined in the compressive sense, and $\boldsymbol{D}$ the rate of deformation tensor, with components

$$D_{ij} = \frac{1}{2}\left(\frac{\partial u_i}{\partial x_j} + \frac{\partial u_j}{\partial x_i}\right). \tag{3.6}$$

Goddard & Lee (2018) have shown that the stress power $\dot{\Phi} = -\boldsymbol{\sigma} : \boldsymbol{D}$ is not always non-negative. Hence, this model is not pursued further. In any case, the bulk viscosity term

vanishes for the velocity field considered here, and their model reduces to the $\mu(I) - \phi(I)$ model.

Another class of models is the higher gradient or 'non-local' models. The stresses at a point depend on the rate of deformation in a spatial region containing that point. There are many types of non-local models (Aranson & Tsimring 2001; Pouliquen *et al.* 2001; Pouliquen & Forterre 2009; Wójcik & Tejchman 2009; Henann & Kamrin 2013; Bouzid *et al.* 2015; Dsouza & Nott 2020) and no single definition fits all of them. For example, Pouliquen *et al.* (2001) and Pouliquen & Forterre (2009) assume that the shear rate at a point depends on the shear rates at other points, whereas Aranson & Tsimring (2001) use an order parameter in the expression for the stress tensor. The order parameter is governed by a differential equation which describes the transition from solid-like to fluid-like behaviour. The model of Wójcik & Tejchman (2009) resembles that of Pouliquen & Forterre (2009), as the shear rate at a point is assumed to be a function of the weighted shear rates at neighbouring points. The models of Henann & Kamrin (2013) and Bouzid *et al.* (2015) are similar to the model of Aranson & Tsimring (2001). Recently, Li & Henann (2019) have shown that the incompressible model of Henann & Kamrin (2013) is well posed. However, the incompressible model of Bouzid *et al.* (2015) is not well posed even though higher gradients are included.

In this paper, the predictions of some of the recent well-posed models are compared with the results of simulations based on the DEM. Ill-posed behaviour is seen only when the models are used to solve the unsteady equations. The present work is an attempt to solve the steady state equations. For the models considered here, even the steady state aspects have not been studied in detail earlier in the context of flow through a vertical channel. It is hoped that the unsteady equations will be examined in the future.

3.1. *Governing equations*

The momentum balances for steady, fully developed flow are given by

$$\frac{\mathrm{d}\sigma_{xx}}{\mathrm{d}x} = 0; \quad \frac{\mathrm{d}\sigma_{xy}}{\mathrm{d}x} = -\rho_p \phi g, \tag{3.7a,b}$$

where σ_{xx} and σ_{xy} are the normal and shear stresses, defined in the compressive sense, ρ_p is the particle density, ϕ is the solids fraction and g is the acceleration due to gravity.

Expressing the stress components in terms of the principal stresses σ_1 and σ_2, we obtain (Sokolovskii 1965; Rao & Nott 2008)

$$\sigma_{xx} = \sigma + \tau\cos(2\psi); \quad \sigma_{yy} = \sigma - \tau\cos(2\psi); \quad \sigma_{xy} = -\tau\sin(2\psi), \tag{3.8a–c}$$

where

$$\sigma = \frac{\sigma_1 + \sigma_2}{2}; \quad \tau = \frac{\sigma_1 - \sigma_2}{2}. \tag{3.9a,b}$$

Here, σ_1 is the major principal stress, and ψ is the inclination of the σ_1-axis relative to the x-axis (figure 1).

Thus (3.7*a*,*b*) and (3.8*a*–*c*) contain one more unknown than the number of equations. Before discussing closure of these equations, it is helpful to consider the more general case of flow parallel to the x–y plane. In classical frictional models (see, for example, Mohan

et al. (1997)), the additional equations are provided by a yield condition

$$\tau = \tau(\sigma, \phi), \tag{3.10}$$

a flow rule

$$\cos(2\psi)\left(\frac{\partial u_y}{\partial y} + \frac{\partial u_x}{\partial x}\right) - \left(\frac{\partial \tau}{\partial \sigma}\right)\left(\frac{\partial u_y}{\partial y} - \frac{\partial u_x}{\partial x}\right) = 0 \tag{3.11}$$

and the coaxiality condition, which enforces the alignment of the principal axes of the stress and rate of deformation tensors

$$\cos(2\psi)\left(\frac{\partial u_x}{\partial y} + \frac{\partial u_y}{\partial x}\right) - \sin(2\psi)\left(\frac{\partial u_y}{\partial y} - \frac{\partial u_x}{\partial x}\right) = 0. \tag{3.12}$$

In particular, (3.11) represents an associated flow rule.

3.2. *The model of Barker et al. (2017)*

Recently, Barker *et al.* (2017) have formulated a model for plane flow that is well posed by incorporating the inertial number I into the frictional equations described above. The coaxiality condition (3.12) is retained, but the yield condition and the flow rule are replaced by

$$\tau = Y(\sigma, \phi, I); \quad \left(\frac{\partial u_x}{\partial x} + \frac{\partial u_y}{\partial y}\right) = f(\sigma, \phi, I)S', \tag{3.13a,b}$$

where S' is an equivalent shear rate, defined by

$$S' = \sqrt{2D'_{ij}D'_{ji}}, \tag{3.14}$$

and

$$D'_{ij} = \frac{1}{2}\left(\frac{\partial u_i}{\partial x_j} + \frac{\partial u_j}{\partial x_i}\right) - \frac{1}{2}\frac{\partial u_k}{\partial x_k}\delta_{ij}. \tag{3.15}$$

Here, repeated indices imply summation, and δ_{ij} is the Kronecker delta. The form of the coaxiality condition given in Barker *et al.* (2017) differs from (3.12), but can be shown to be equivalent after some manipulations. The alternative form is also discussed in § 3 of Barker *et al.* (2017).

Because of the incorporation of I, (3.13*a*,*b*) does not represent classical frictional behaviour. However, for ease of exposition, we retain the terms 'yield condition' and 'flow rule'.

For the equations to be well posed, the yield function Y and flow rule function f are required to satisfy certain conditions. To relate these equations to the $\mu(I)$ model, Barker *et al.* (2017) proposed the forms

$$\left.\begin{aligned} \tau = Y(\sigma, \phi, I) &= \alpha(I)\sigma - \frac{\sigma^2}{C(\phi)} \\ f(\sigma, \phi, I) &= \beta(I) - \frac{2\sigma}{C(\phi)} \end{aligned}\right\}, \tag{3.16}$$

where σ is the mean stress defined by (3.9*a*,*b*) and

$$\left.\begin{aligned} \alpha(I) &= \frac{4}{5}\mu(I) + \frac{12}{25} I^{-2/5} \int_0^I j^{-3/5}\mu(j)\,\mathrm{d}j \\ \beta(I) &= -\frac{2}{5}\mu(I) + \frac{24}{25} I^{-2/5} \int_0^I j^{-3/5}\mu(j)\,\mathrm{d}j \\ C(\phi) &= \Lambda \frac{\phi - \phi_{min}}{\phi_{max} - \phi}, \end{aligned}\right\} \tag{3.17}$$

where Λ, ϕ_{min} and $\phi_{max} > \phi_{min}$ are material constants. The form suggested by Barker *et al.* (2017) for $C(\phi)$ is only representative of a function that increases monotonically with ϕ, and has not been deduced from experimental data. It is identical in form to the expression proposed by Savage & Sayed (1979) for the mean stress at a critical state or a state of isochoric deformation.

For the problem at hand, the coaxiality condition (3.12) reduces to

$$\frac{\mathrm{d}u_y}{\mathrm{d}x}\cos(2\psi) = 0, \tag{3.18}$$

and (3.2) to

$$I = \frac{d_p \dfrac{\mathrm{d}u_y}{\mathrm{d}x}}{\sqrt{\sigma_{xx}/\rho_p}}, \tag{3.19}$$

where the shear rate S and the normal stress N in (3.2) have been identified with $\mathrm{d}u_y/\mathrm{d}x$ and σ_{xx}, respectively. Similarly, (3.4) is replaced by

$$\mu(I) = \frac{|\sigma_{xy}|}{\sigma_{xx}}. \tag{3.20}$$

As noted by Mohan *et al.* (1997), either (i) $\mathrm{d}u_y/\mathrm{d}x = 0$, or (ii) $\psi = \pm\pi/4$. If (i) holds, the material moves as a plug, and there are no shear layers near the walls of the channel. This is at variance with experimental observations and the results of DEM simulations. Hence, this root must be discarded, except possibly for a plug layer near the centre of the channel.

Considering the other roots (ii), the choice $\psi = -\pi/4$ is ruled out as it implies that $\sigma_{xy} = \tau \geqslant 0$. Hence, if $\tau \neq 0$ at the wall $x = W$, the material flowing downward will exert an upward shear stress on the wall. This behaviour is unrealistic and must be avoided.

The other choice is $\psi = \pi/4$, which along with (3.8*a*–*c*) implies that

$$\sigma_{xx} = \sigma_{yy} = \sigma; \quad \sigma_{xy} = -\tau. \tag{3.21a,b}$$

At the centre $x = 0$, the velocity profile must be symmetric, and hence $\mathrm{d}u_y/\mathrm{d}x = 0$. Similarly, the shear stress $-\sigma_{xy}(x = 0) = \tau(x = 0) = 0$. Equation (3.19) implies that $I(0) = 0$, and the data of Jop, Forterre & Pouliquen (2005) show that $\mu(0) = \mu_s > 0$. It follows from (3.20) that $\tau(0) = \mu_s\sigma(0) = 0$, or $\sigma(0) = 0$. However, the momentum balance (3.7*a*,*b*) and this result imply that $\sigma_{xx} = \sigma = 0$ even at the wall, which is unrealistic. Hence, neither of the roots $\mathrm{d}u_y/\mathrm{d}x = 0$ and $\psi = \pi/4$ apply throughout the domain $0 < x < W$.

One approach to resolve this problem is to postulate a plug layer of thickness x_p near the centre, where $\mathrm{d}u_y/\mathrm{d}x = 0$, and a shear layer of thickness $(W - x_p)$ near the wall. In the

shear layer, $\psi = \pi/4$ and appropriate matching conditions are used at the interface $x = x_p$. A similar approach was used by Mohan *et al.* (1997) for the frictional-kinetic equations.

In the plug layer ($0 \leqslant x \leqslant x_p$), the material does not deform and the solids fraction ϕ is assumed to be a constant $\equiv \phi_p$. The momentum balances imply that

$$\left.\begin{aligned} \sigma_{xx} = \text{const.} = \sigma + \tau\cos(2\psi) \equiv N \\ -\sigma_{xy} = \tau\sin(2\psi) = (\rho_p g \phi_p)x \end{aligned}\right\}. \tag{3.22}$$

In the shear layer ($x_p < x \leqslant W$), $\psi = \pi/4$ and the momentum balances reduce to

$$\left.\begin{aligned} \sigma_{xx} = \text{const.} = \sigma = N \\ \frac{\mathrm{d}\tau}{\mathrm{d}x} = \rho_p \phi g \end{aligned}\right\}, \tag{3.23}$$

where (3.21*a*,*b*) has been used. As $\partial u_k/\partial x_k = 0$, the flow rule (3.13*b*) reduces to $f = 0$, or using (3.16)

$$\sigma = N = \beta(I) C(\phi)/2. \tag{3.24}$$

Applying the above conditions and using (3.16)

$$\tau = Y(\sigma, \phi, I) = \mu(I)\sigma = \mu(I) N. \tag{3.25}$$

An explicit expression is needed for $\mu(I)$; here, we use the expression of Jop, Forterre & Pouliquen (2005), which is given by

$$\mu(I) = \mu_s + \frac{\Delta\mu}{(I_0/I) + 1}, \tag{3.26}$$

where μ_s, $\Delta\mu$, and I_0 are positive constants. Equation (3.24) is linear in ϕ, and can be solved to obtain

$$\phi = \frac{\beta(I)\Lambda\phi_{min} + 2N\phi_{max}}{\beta(I)\Lambda + 2N}. \tag{3.27}$$

Using (3.27), (3.17) and (3.26), (3.23) is integrated from $x = x_p$ to $x = W$ with the initial condition $I(x = x_p) = 0$. The MATLAB routine ODE45 is used for numerical integration, and the integral in the expression for $\beta(I)$ in (3.17) is evaluated using Gauss–Legendre four point quadrature. In the limit $I \to 0$, the integral can be evaluated analytically, giving $\beta(I) = 2\mu_s$.

To obtain the thickness x_p of the plug layer, the stresses and the velocity gradient at x_p^- must be matched to the corresponding values at x_p^+. At $x = x_p$, $I(x_p) = 0$ and

$$\begin{aligned} -\sigma_{xy}(x = x_p^-) = (\rho_p \phi_p g) x_p = -\sigma_{xy}(x = x_p^+) \\ = \tau = \mu(I(x = x_p))\sigma = \mu(I(x = x_p))N. \end{aligned} \tag{3.28}$$

As $I(x_p^-) = 0$, (3.26) and (3.28) imply that $\mu(x = x_p) = \mu_s$. Substituting $I = 0$, ϕ_p can be obtained from (3.27), and hence

$$x_p = \frac{\mu_s N}{\rho_p \phi_p g}. \tag{3.29}$$

Equation (3.19) implies that the velocity profile is governed by

$$\frac{\mathrm{d}u_y}{\mathrm{d}x} = \frac{I}{d_p}\sqrt{\frac{N}{\rho_p}}. \tag{3.30}$$

As there is one unknown parameter, namely, the normal stress N, and one condition is needed to integrate (3.30), two conditions have to be specified. Here, the bulk solids

fraction

$$\bar{\phi} \equiv \frac{1}{W}\int_0^W \phi \, \mathrm{d}x, \tag{3.31}$$

and the mass flow rate

$$\dot{M} \equiv 2\rho_p B \int_0^W (-u_y)\phi \, \mathrm{d}x, \tag{3.32}$$

where B is the thickness of the channel in the z-direction (figure 1), are matched to the DEM results.

In the DEM, $\dot{M}$ is fixed by specifying $\bar{\phi}$ for a fixed value of $2\,W$, but it appears that for the continuum models, both the parameters can be specified independently. In the latter case, the additional degree of freedom arises because we are unaware of a suitable velocity or stress boundary condition (b.c.) that can be specified at the wall.

For example, a modified form of the b.c. proposed by Mohan *et al.* (1999) is given by

$$u_y(x = W) - u_{wall} = -l_u \frac{\mathrm{d}u_y}{\mathrm{d}x}, \tag{3.33}$$

where u_{wall} is the velocity of the wall and l_u is a material parameter called the slip length. In our case, $u_{wall} = 0$. Equation (3.33) is due to Tejchman & Gudehus (1993) and Tejchman & Wu (1993), who expressed it in terms of displacement and rotation. Subsequently, Mohan *et al.* (1999, 2002) rewrote it in terms of the velocity and the angular velocity ω. As noted by Batchelor (1967), ω is equal to half the vorticity $\mathrm{d}u_y/\mathrm{d}x$ for a classical continuum. However, the value of l_u is not known *a priori*. Hence it is calculated using (3.33) after the velocity field has been obtained. We shall see later that l_u varies with $\bar{\phi}$ and the channel width $2\,W$ for the models used here, and hence (3.33) is not a realistic b.c. for most of the models.

There are similar reservations about the wall friction b.c.

$$\mu(x = W) = \mu_w = \frac{-\sigma_{xy}(x = W)}{N} = \frac{\tau(x = W)}{N} = \tan\delta, \tag{3.34}$$

where (3.21*a*,*b*) has been used and δ is called the angle of wall friction. Equation (3.34) has been commonly used in the in the literature on slow flow (Brennen & Pearce 1978; Nedderman *et al.* 1982; Dsouza & Nott 2020) but may not be appropriate when the inertial effects are important near the wall. Integrating the second of (3.7*a*,*b*) from $x = 0$ to $x = W$ using an initial condition $\sigma_{xy}(x = 0) = 0$, and using (3.31) and (3.34)

$$\tan\delta = \frac{\bar{\phi}}{\tilde{N}}, \tag{3.35}$$

where $\tilde{N} = N/(\rho_p g W)$.

The model of Barker *et al.* (2017) differs from $\mu(I) - \phi(I)$ model as it is shown to be well posed, and (3.27) implies that ϕ depends on I and the normal stress N.

3.3. *The model of Schaeffer et al. (2019)*

This builds on the work of Barker *et al.* (2017), by proposing an *ad hoc* expression for the yield function Y and deducing the expression for the flow rule function f. It is shown that the resulting equations are well posed. Thus this model involves fewer assumptions than that of Barker *et al.* (2017), as the latter proposes *ad hoc* expressions for both Y and f.

Schaeffer *et al.* (2019) conducted gravity-free DEM simulations of the plane shear of discs, and found that $\mu = \mu(I)$. They fitted the data to (3.26), thereby determining the values of μ_s, $\Delta\mu$ and I_0. They also found that

$$I = \Psi(\phi) \equiv \frac{\phi_c - \phi}{a}, \tag{3.36}$$

where ϕ_c and a are constants. We shall use different data for parameter estimation as our grains are assumed to be spherical.

Retaining the coaxiality condition (3.12), a new yield condition dependent on I, σ and Ψ is chosen as

$$\tau = Y(\sigma, I, \phi) = \mu(\Psi(\phi))\sigma\frac{I}{\Psi(\phi)}. \tag{3.37}$$

Note that $I \neq \Psi(\phi)$ in general. The $\mu(I) - \phi(I)$ model is recovered in cases where $I = \Psi(\phi)$. To make the system well posed, it turns out that (Barker *et al.* 2017)

$$f(\sigma, I, \phi) = f(I, \phi) = \frac{1}{4}\,\mu(\Psi(\phi))\left(\frac{I}{\Psi(\phi)} - \frac{\Psi(\phi)}{I}\right). \tag{3.38}$$

For steady, fully developed flow $\partial u_k/\partial x_k = 0$. Hence, (3.13*b*) and (3.38) imply that

$$I = \Psi(\phi). \tag{3.39}$$

Using (3.36), we obtain

$$\phi = \phi_c - aI. \tag{3.40}$$

For this special case, the model of Schaeffer *et al.* (2019) is identical to the $\mu(I) - \phi(I)$ model. However, they have shown that for unsteady one-dimensional flow, the model leads to well-posed behaviour of the numerical solutions, in contrast to the $\mu(I) - \phi(I)$ model.

To the best of our knowledge, the only other papers that have applied the $\mu(I) - \phi(I)$ model to channel flow are those of Pouliquen *et al.* (2001) and Pouliquen *et al.* (2006). The present work differs from theirs in the following respects: (i) they use a no-slip condition at the wall, whereas we permit slip, (ii) they state that the shear stress τ and hence the friction coefficient $\mu = \tau/N$ vary linearly with x, whereas we find that this is not an exact result but holds to a good approximation, (iii) results are presented here for a range of channel widths $2\,W$ and bulk solids fractions $\bar{\phi}$, but only for one value of $\bar{\phi}$ and an unspecified value of $2\,W$ in their work, (iv) as experimental data and DEM results were not available at that time, model predictions could not be compared with these in their work, whereas extensive comparisons with DEM results are presented here. However, we greatly appreciate their efforts to solve this problem.

Using (3.26) and (3.40), and noting that $\tau = \mu(I)N$, the momentum balance (3.23) is integrated from x_p to W with the initial condition $I(x = x_p) = 0$. The solids fraction in the plug layer is given by $\phi_p = \phi_c$ as $I = 0$ (see (3.36) and the thickness of the plug layer is given by (3.29). This implicitly assumes that the DEM results used to deduce the forms of $\mu(I)$ and $\phi(I)$ are valid in the limit $I \to 0$, even though the smallest value of I for the results is about 0.002. The form (3.40) permits the momentum balance (3.23) to be integrated analytically, resulting in

$$\frac{1}{(I_0 + (\phi_c/a))^2}\ln\left|\frac{I_0 + I}{(\phi_c/a) - I}\right| - \frac{1}{(I_0 + (\phi_c/a))(I_0 + I)} = \frac{a}{I_0\Delta\mu}\frac{\rho_p g x}{N} + k, \tag{3.41}$$

where the integration constant k is evaluated by using the initial condition $I(x_p) = 0$. The solids fraction is obtained using (3.40), and N by matching $\bar{\phi}$ to the DEM result. To obtain the velocity profile, (3.30) is integrated using (3.41) similarly, as discussed in § 3.2.

3.4. *The model of Henann & Kamrin (2013)*

For three-dimensional flow, Henann & Kamrin (2013) define an equivalent shear stress by

$$\tau' = (\sigma'_{ij}\sigma'_{ji}/2)^{1/2}, \tag{3.42}$$

where

$$\sigma'_{ij} \equiv \sigma_{ij} - p\delta_{ij}; \quad p \equiv \sigma_{kk}/3, \tag{3.43a,b}$$

and p is the mean stress or the pressure. Their constitutive equation is given by

$$\sigma_{ij} = p\delta_{ij} - 2\frac{p}{f} D_{ij}, \tag{3.44}$$

where the stresses are defined in the compressive sense and the quantity f is called the granular fluidity. It is defined by

$$f \equiv S'/\mu, \tag{3.45}$$

where the shear rate S' is defined by (3.14), with (3.15) replaced by

$$D'_{ij} = \frac{1}{2}\left(\frac{\partial u_i}{\partial x_j} + \frac{\partial u_j}{\partial x_i}\right) - \frac{1}{3}\frac{\partial u_k}{\partial x_k}\delta_{ij}, \tag{3.46}$$

and

$$\mu \equiv \tau'/p. \tag{3.47}$$

Here, τ' is given by (3.42).

Because f is governed by a differential equation, this model is called a non-local model in the sense of GDR-MiDi (2004). At a steady state, this equation is assumed to be given by (Kamrin & Henann 2015; Zhang & Kamrin 2017)

$$A^2 d_p^2 \nabla^2 f = \Delta\mu\left(\frac{\mu_s - \mu}{\mu_s + \Delta\mu - \mu}\right) f + \frac{\Delta\mu}{I_0}\sqrt{\frac{\rho_p d_p^2}{p}}\,\mu f^2, \tag{3.48}$$

where I_0, $\Delta\mu$, μ_s and A are constants.

Equation (3.48) differs from the equation used by Kamrin & Koval (2012) and Henann & Kamrin (2013), who linearized the term involving f^2 about a local value of the fluidity f_{loc}. The latter was assumed to be a function of the inertial number I. As suggested by one of the referees, we use the more complete form (3.48). Thus the present analysis deals with a modified version of the model of Henann & Kamrin (2013). They assume that $\phi =$ const., which is a drawback of the model. They suggested that ϕ could be treated as a function of I, thereby relaxing this constraint. However, it was not implemented in their paper. Some results obtained with $\phi = \phi(I)$ are presented here.

Let us now consider the case of steady, fully developed flow. Equation (3.44) implies that

$$\sigma_{xx} = \sigma_{yy} = \sigma_{zz} = p; \quad \sigma_{xy} = \sigma_{yx} = -\frac{p}{f}\frac{\mathrm{d}u_y}{\mathrm{d}x}. \tag{3.49a,b}$$

Using (3.49*a*,*b*), the momentum balances reduce to

$$p = \text{const.} \equiv N; \quad \frac{\mathrm{d}}{\mathrm{d}x}\left(\frac{p}{f}\frac{\mathrm{d}u_y}{\mathrm{d}x}\right) = \rho_p \phi g. \tag{3.50a,b}$$

Integrating (3.50*b*) with $\phi = \text{const.} = \phi_p$ and using the b.c. of vanishing shear stress at $x = 0$, we obtain

$$\frac{N}{f}\frac{\mathrm{d}u_y}{\mathrm{d}x} = \rho_p \phi_p g x. \tag{3.51}$$

Henceforth, ϕ_p is set equal to the bulk solids fraction $\bar{\phi}$ obtained from the DEM results.

Using (3.42), (3.47), (3.49*a*,*b*) and (3.51), we obtain

$$\mu = \frac{|\sigma_{xy}|}{p} = \left|\frac{1}{f}\frac{\mathrm{d}u_y}{\mathrm{d}x}\right| = \frac{1}{f}\frac{\mathrm{d}u_y}{\mathrm{d}x} = \frac{\rho_p \phi_p g}{N} x, \tag{3.52}$$

as $\mathrm{d}u_y/\mathrm{d}x$ is expected to be $\geqslant 0$ for downward flow, and f should be non-negative (see (3.45)).

The equation for the fluidity (3.48) reduces to

$$\frac{\mathrm{d}^2 f}{\mathrm{d}x^2} = \frac{\Delta\mu}{A^2 d_p^2}\left(\frac{\mu_s - \mu}{\mu_s + \Delta\mu - \mu}\right) f + \frac{\Delta\mu}{I_0 A^2 d_p^2}\sqrt{\frac{\rho_p d_p^2}{N}}\mu f^2. \tag{3.53}$$

Two b.c.s are needed for (3.53). Henann & Kamrin (2013) assume that the gradient of f in the direction normal to a boundary vanishes. Here, it implies that $\mathrm{d}f/\mathrm{d}x = 0$ at the walls $x = \pm W$. As (3.53) is solved only in the region $0 \leqslant x \leqslant W$, let us consider the b.c. at $x = 0$ first. The vertical velocity u_y is expected to be an even function of x. Expanding u_y in a Taylor series about $x = 0$, we obtain

$$u_y = a + bx^2 + O(x^4); \quad x \to 0, \tag{3.54}$$

where a and b are constants. Hence the shear rate S' is given by $S' = 2bx + O(x^3)$. Using this result along with (3.45) and (3.52), we obtain

$$f = \frac{2b}{c} + O(x^2); \quad x \to 0, \tag{3.55}$$

where c is a constant. Hence one b.c. is given by

$$\frac{\mathrm{d}f}{\mathrm{d}x}(0) = 0. \tag{3.56}$$

As a physically appealing b.c. is lacking at $x = W$, we follow Zhang & Kamrin (2017) and set

$$f(x = W) \equiv f_w = f_{dem}, \tag{3.57}$$

where f_{dem} is the value of f obtained from the DEM results. By analogy with the slip b.c. (3.33), a possible alternative b.c. for f_w may be

$$f_w = l_f \left|\frac{\mathrm{d}f}{\mathrm{d}x}\right|, \tag{3.58}$$

where l_f is a slip length associated with the fluidity. Values of l_f are obtained from the DEM results and the model predictions, as discussed in § 4.4.

The MATLAB routines ODE45 and FSOLVE are used to integrate (3.53) and for iterative matching of the b.c.s, respectively. Here, ϕ_p is chosen as $\bar{\phi}$, which is consistent with the selection for comparisons with the DEM and the other models. To obtain the velocity profile, (3.51) has to be integrated, and two more conditions are needed as the normal stress N is not known *a priori*. Because of the lack of appropriate b.c., N and the mass flow rate $\dot{M}$ are matched to the DEM results. The structure of (3.53) and the b.c. permits an approximate solution, as discussed in § 4.4.2.

To relax the assumption that $\phi = \text{const.}$, some results are also presented with $\phi = \phi(I)$, where the functional form (3.40) is used. The equations will be solved in similarly, as discussed in § 3.2, and N will be predicted by matching $\bar{\phi}$ to the DEM results.

As noted by one of the referees, (3.53) has been solved earlier by Zhang & Kamrin (2017). However, the friction coefficient μ has been taken from the DEM results (K. Kamrin, private communication 2021), and hence it is not a complete solution of the model equations (3.49*a*,*b*), (3.50*a*,*b*), (3.52) and (3.53). There is no mention of the ϕ and u_y profiles in their paper, a gap that has been filled in the present work. Some other aspects of this model are discussed in § 4.4.

3.5. *The model of Dsouza & Nott (2020)*

Dsouza & Nott (2020) start with the classical frictional model that involves a yield condition and a flow rule (Srivastava & Sundaresan 2003; Rao & Nott 2008). Integrating the flow rule over a representative volume with an effective radius ℓ, and ignoring terms of $O(\ell^4)$ and higher in the stresses, the constitutive equations are given by

$$\left.\begin{aligned} \sigma_{ij} &= p\delta_{ij} - \frac{2\mu_*}{S'}(p_c D'_{ij} - \ell^2 \Pi \nabla^2 D'_{ij}) \\ p_c &= \Pi - \ell^2 \frac{\mathrm{d}\Pi}{\mathrm{d}\phi}\nabla^2\phi \\ p &= p_c\left(1 - \frac{\mu_b}{S'}\boldsymbol{\nabla}\cdot\boldsymbol{u}\right) + \ell^2\Pi\frac{\mu_b}{S'}\nabla^2\,\boldsymbol{\nabla}\cdot\boldsymbol{u} \end{aligned}\right\}, \tag{3.59}$$

where μ_* and μ_b are constants, S' is defined by (3.14), D'_{ij} by (3.46), $\boldsymbol{u}$ is the velocity vector and $p = \sigma_{kk}/3$ is the mean stress or the pressure. The variable p_c in (3.59) is the mean stress at a critical state or a state of isochoric motion, and $\Pi(\phi)$ is its 'local' contribution. A suitable form must be specified for $\Pi(\phi)$, and it is chosen as (Savage & Sayed 1979)

$$\Pi(\phi) = \Lambda^* \frac{\phi - \phi_{min}}{\phi_{max} - \phi},\ \phi \geqslant \phi_{min}; \quad \Pi = 0,\ \phi \leqslant \phi_{min}, \tag{3.60}$$

where Λ^*, ϕ_{min} and $\phi_{max} > \phi_{min}$ are material constants. Dsouza & Nott (2020) use the expression proposed by Johnson, Nott & Jackson (1990)

$$\Pi(\phi) = \Lambda' \frac{(\phi - \phi_{min})^2}{(\phi_{max} - \phi)^5},\ \phi \geqslant \phi_{min}; \quad \Pi = 0,\ \phi \leqslant \phi_{min}, \tag{3.61}$$

where Λ' is a material constant. The latter form diverges faster as $\phi \to \phi_{max}$ than the former. Here, we use (3.60) to solve this model. The effect of (3.61) on the predictions is discussed in § 4.

Because of the integration of the flow rule over a volume, (3.59) may be regarded as a non-local model. The authors state, but do not prove, that the model is linearly well posed.

As $\nabla \cdot \boldsymbol{u} = 0$ for the velocity field (1.2*a*,*b*), (3.59) reduces to

$$\left.\begin{aligned} \sigma_{xx} = \sigma_{yy} = \sigma_{zz} = p = p_c = \Pi - \ell^2 \frac{\mathrm{d}\Pi}{\mathrm{d}\phi}\frac{\mathrm{d}^2\phi}{\mathrm{d}x^2} \\ \sigma_{xy} = \sigma_{yx} = -\frac{\mu_*}{S'}\left(p_c \frac{\mathrm{d}u_y}{\mathrm{d}x} - \ell^2 \Pi \frac{\mathrm{d}^3 u_y}{\mathrm{d}x^3}\right) \end{aligned}\right\}, \tag{3.62}$$

where

$$S' = \frac{\mathrm{d}u_y}{\mathrm{d}x}. \tag{3.63}$$

Using (3.62), the momentum balances reduce to

$$\left.\begin{aligned} p = p_c = \Pi - \ell^2 \frac{\mathrm{d}\Pi}{\mathrm{d}\phi}\frac{\mathrm{d}^2\phi}{\mathrm{d}x^2} = \text{const.} \equiv N \\ \frac{\mathrm{d}\sigma_{xy}}{\mathrm{d}x} = -\frac{\mathrm{d}}{\mathrm{d}x}\left(\frac{\mu_*}{S'}\left(p_c \frac{\mathrm{d}u_y}{\mathrm{d}x} - \ell^2 \Pi \frac{\mathrm{d}^3 u_y}{\mathrm{d}x^3}\right)\right) = -\rho_p \phi g \end{aligned}\right\}. \tag{3.64}$$

To solve (3.64), seven conditions are needed as the normal stress N is unknown *a priori*. The first of (3.64) depends only on ϕ, and hence is solved separately using the MATLAB routine ODE45. Due to the lack of appropriate b.c. for ϕ, we match the bulk solids fraction $\bar{\phi}$ and $\phi(0)$ to the DEM results. As the ϕ profile is expected to be symmetric about $x = 0$, we have $\mathrm{d}\phi/\mathrm{d}x(0) = 0$.

Four b.c.s are needed to solve the second of (3.64). The velocity profile is expected to be symmetric about $x = 0$, and hence $\mathrm{d}u_y/\mathrm{d}x(0) = 0$. As the shear stress $\sigma_{xy}(0) = 0$, (3.62) and the condition $\mathrm{d}u_y/\mathrm{d}x(0) = 0$ imply that

$$\Pi \frac{\mathrm{d}^3 u_y}{\mathrm{d}x^3}(0) = 0, \tag{3.65}$$

where Π is given by the last of (3.59). Thus either (i) $\Pi(\phi) = 0$, or (ii) $\mathrm{d}^3 u_y/\mathrm{d}x^3 = 0$. The root (i) implies that ϕ has a minimum at $x = 0$, a condition that is at variance with our DEM results and qualitative experimental observations of low ϕ values near the wall. Hence, root (ii) is chosen and

$$\frac{\mathrm{d}^3 u_y}{\mathrm{d}x^3}(0) = 0. \tag{3.66}$$

The two additional b.c.s required are obtained by matching the mass flow rate $\dot{M}$ and $u_y(0)$ to the DEM results.

Integrating the second of (3.64) once, we obtain

$$\left.\frac{\mu_*}{S'}\left(p_c \frac{\mathrm{d}u_y}{\mathrm{d}x} - \ell^2 \Pi \frac{\mathrm{d}^3 u_y}{\mathrm{d}x^3}\right)\right|_x = \rho_p g \int_0^x \phi \, \mathrm{d}x'. \tag{3.67}$$

With the profile of ϕ at hand, we use a three-point central difference scheme for $q = \mathrm{d}u_y/\mathrm{d}x$ on the left-hand side and numerical integration (trapezoidal rule) for the integral on the right-hand side to solve (3.67). Once q is known, u_y is evaluated using a two-point central difference scheme.

There is a flaw in this argument, as (3.63) and the b.c. $\mathrm{d}u_y/\mathrm{d}x(0) = 0$ imply that $S'(0) = 0$. Hence the b.c. (3.66) implies that $\sigma_{xy}(0)$ becomes indeterminate. As an *ad hoc* measure,

we replace the dimensionless shear rate $\tilde{S} = S'\sqrt{W/g}$ by $\tilde{S} + \tilde{\epsilon}$, where $\tilde{\epsilon}$ is a small positive constant. The actual value used, and sensitivity to changes in its value, will be discussed in § 4. This issue merits further attention.

The structure of (3.64) and the b.c. permits an approximate solution, as discussed in § 4.5.2.

3.6. *Comparison of the models*

The constitutive equations and model parameters are listed in table 1. The stresses depend on ϕ and the velocity gradients for the first two models. They incorporate the effect of ϕ, unlike the models of Jop, Forterre & Pouliquen (2006) and Henann & Kamrin (2013), and well-posed models are derived without including higher gradients of the velocity. All the models involve a material length scale, either through the inertial number I, the fluidity f or the radius of the averaging volume ℓ. Hence, they are able to predict the occurrence of shear layers. The model of Henann & Kamrin (2013) assumes that ϕ is a constant, and involves the second derivatives of the fluidity f. In the model of Dsouza & Nott (2020), the stresses depend on the second derivatives of ϕ, and the third derivatives of the velocity. Such models require the specification of additional b.c.s, which is an open problem at present. The b.c.s listed in table 1 are used in conjunction with the DEM results to check whether l_u, δ, and l_f are material parameters.

3.7. *Parameter values*

In the model of Barker *et al.* (2017), the parameters used are ϕ_{max}, ϕ_{min}, Λ, μ_s, $\Delta\mu$ and I_0. The values of ϕ_{max} and ϕ_{min} used by Johnson *et al.* (1990) are 0.65 and 0.50, respectively, but the functional form is different. We set $\phi_{max} = \phi_{drp} = 0.64$, where ϕ_{drp} denotes the solids fraction corresponding to dense random packing. This value has been deduced from measurements on steel balls (Scott 1960; Scott & Kilgour 1969) and simulations of frictionless hard-sphere fluids (Berryman 1983). Similarly, ϕ_{min} is chosen as $\phi_f = 0.49$, the freezing solids fraction (Hoover & Ree 1968) obtained from simulations of hard-sphere fluids. Below ϕ_{min}, it is assumed that there are no sustained frictional contacts. Chialvo *et al.* (2012) performed DEM simulations of the gravity-free plane shear of spheres for inertial numbers in the range 10^{-5}–10^{0}. Fitting (3.26) to their data (figure 2*a*), we obtain $\mu_s = 0.38$, $\Delta\mu = 0.55$ and $I_0 = 0.29$.

Let us now discuss the estimation of the parameter Λ which occurs in (3.17). As $\partial u_k/\partial x_k = 0$, the quantity σ in (3.24) is the mean stress at a critical state, which may be denoted by σ_c. Thus $\sigma_c = \beta(I)C(\phi)/2$. In the limit of quasistatic flow ($I \to 0$), $\beta(I) = 2\mu_s$ as discussed earlier. Hence $C(\phi) = \sigma_c/\mu_s$ in this limit. Using (3.17), Λ can be estimated if data is available for the variation of σ_c with ϕ for quasistatic flow. Fickie, Mehrabi & Jackson (1989) measured ϕ along the centreline of a wedge-shaped hopper through which glass beads were flowing. Jyotsna & Rao (1997) used an approximate expression for ϕ to fit the data and hence estimated the parameters in their expression for $\sigma_c(\phi)$. The results are shown by the circles in figure 2(*b*), and are assumed to be valid for quasistatic flow. Fitting (3.17) to this 'data', Λ is found to be 555 N m^{-2}. The fit, shown by the dashed curve in figure 2(*b*), is reasonable but not very good. Unfortunately, the range of ϕ values for which the data are available is very narrow.

The model of Dsouza & Nott (2020) involves the local value of the mean stress at a critical state $\Pi(\phi)$. The quantities $\Pi = (\sigma_{xx} + \sigma_{yy} + \sigma_{zz})_c/3$ and $\sigma_c = (\sigma_{xx} + \sigma_{yy})_c/2$ differ in general, even though both are defined for a critical state, which is denoted by the subscript c. For the model of Barker *et al.* (2017), $\sigma_{xx} = \sigma_{yy}$, but σ_{zz} is undefined. On the

Model	Constitutive equations	Parameters	Wall b.c.
	$\tau = \alpha(I)\sigma - \dfrac{\sigma^2}{C(\phi)}$	$\mu_s, \Delta\mu, I_0$	—
	$f(\sigma, \phi, I) = \beta(I) - \dfrac{2\sigma}{C(\phi)}$	$\Lambda, \phi_{min}, \phi_{max}$	—
Barker *et al.* (2017)	$\alpha(I) = \dfrac{4}{5}\mu(I)$		$u_y(x = W) = -l_u \dfrac{\mathrm{d}u_y}{\mathrm{d}x}$
	$+\dfrac{12}{25} I^{-2/5} \displaystyle\int_0^I j^{-3/5}\mu(j)\,\mathrm{d}j$	—	$\mu_w = \dfrac{\tau(x = W)}{N} = \tan\delta$
	$\beta(I) = -\dfrac{2}{5}\mu(I)$		
	$+\dfrac{24}{25} I^{-2/5} \displaystyle\int_0^I j^{-3/5}\mu(j)\,\mathrm{d}j$	—	—
	$C(\phi) = \Lambda \dfrac{\phi - \phi_{min}}{\phi_{max} - \phi},$	—	—
	$\mu(I) = \mu_s + \dfrac{\Delta\mu}{(I_0/I) + 1}$	—	—
	$\Psi(\phi) \equiv \dfrac{\phi_c - \phi}{a}$	$\mu_s, \Delta\mu, I_0$	—
Schaeffer *et al.* (2019)	$\tau = \mu(\Psi(\phi))\sigma \dfrac{I}{\Psi(\phi)}$	ϕ_c, a	—
	$f(\sigma, I, \phi)$		$u_y(x = W) = -l_u \dfrac{\mathrm{d}u_y}{\mathrm{d}x}$
	$= \dfrac{1}{4}\,\mu(\Psi(\phi))\left(\dfrac{I}{\Psi(\phi)} - \dfrac{\Psi(\phi)}{I}\right)$	—	$\mu_w = \dfrac{\tau(x = W)}{N} = \tan\delta$
	$\mu(\Psi(\phi)) = \mu_s + \dfrac{\Delta\mu}{(I_0/\Psi(\phi)) + 1}$	—	—
Henann & Kamrin (2013)	$\sigma_{ij} = p\delta_{ij} - 2\dfrac{p}{f} D_{ij}$	$\mu_s, \Delta\mu, I_0$	$u_y(x = W) = -l_u \dfrac{\mathrm{d}u_y}{\mathrm{d}x}$
	$A^2 d_p^2 \nabla^2 f = \Delta\mu \left(\dfrac{\mu_s - \mu}{\mu_s + \Delta\mu - 144\mu}\right) f$	A	$f_w = l_f \left\lvert \dfrac{\mathrm{d}f}{\mathrm{d}x} \right\rvert$
	$+\dfrac{\Delta\mu}{I_0}\sqrt{\dfrac{\rho_p d_p^2}{p}}\,\mu f^2$	—	$\mu_w = \dfrac{\tau(x = W)}{N} = \tan\delta$
	$\sigma_{ij} = p\delta_{ij}$	μ_*, μ_b	—
	$-\dfrac{2\mu_*}{S'}(p_c D'_{ij} - \ell^2 \Pi \nabla^2 D'_{ij})$	—	—
Dsouza & Nott (2020)	$p_c = \Pi - \ell^2 \dfrac{\mathrm{d}\Pi}{\mathrm{d}\phi} \nabla^2\phi$	$\Lambda^*, \phi_{min}, \phi_{max}$	—
	$p = p_c \left(1 - \dfrac{\mu_b}{S'} \boldsymbol{\nabla \cdot u}\right)$	ℓ	—
	$+\ell^2 \Pi \dfrac{\mu_b}{S'} \nabla^2 \boldsymbol{\nabla \cdot u}$		$u_y(x = W) = -l_u \dfrac{\mathrm{d}u_y}{\mathrm{d}x}$
	$\Pi(\phi) = \Lambda^* \dfrac{\phi - \phi_{min}}{\phi_{max} - \phi}, \phi \geqslant \phi_{min}$	—	$\mu_w = \dfrac{\tau(x = W)}{N} = \tan\delta$
	$\Pi = 0, \phi \leqslant \phi_{min}$	—	—

Table 1. Models, parameters and b.c.s at the wall ($x = W$).

other hand, the model of Dsouza & Nott (2020) implies that $\sigma_{xx} = \sigma_{yy} = \sigma_{zz}$. Ignoring this complication, Π is fitted to the circles in figure 2(*b*) using (3.60) and (3.61). The result is $\Lambda^* = 211$ N m^{-2} and $\Lambda' = 0.0988$ N m^{-2}. Equation (3.61) fits the data better but (3.60) will be used here. The effect of using (3.61) is discussed in § 4.5. For the model of Schaeffer *et al.* (2019), ϕ_c and a are obtained by fitting (3.40) to our DEM data for I in the range 0.002–0.2 (figure 2*c*). The result is $\phi_c = 0.613$ and $a = 0.31$.

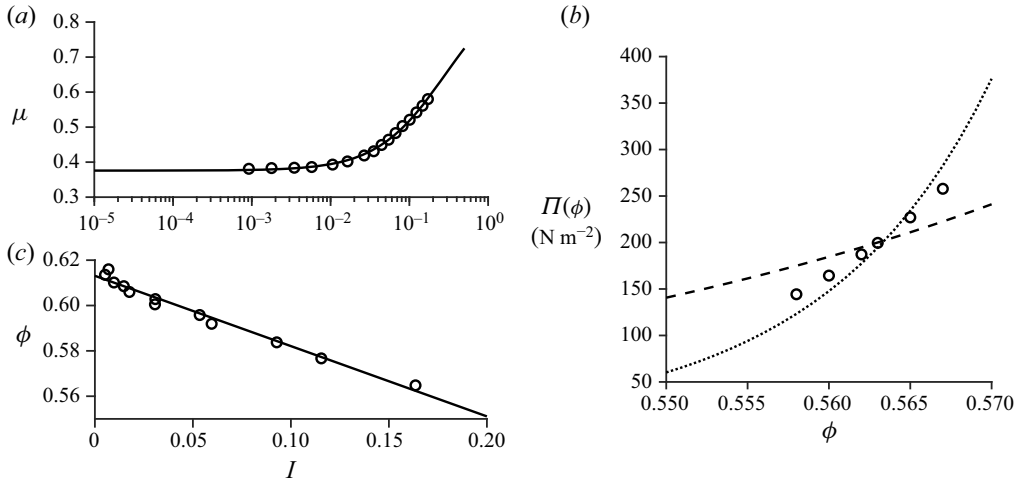

Figure 2. Estimation of parameters: (*a*) ○, data of Chialvo *et al.* (2012); —, (3.26), (*b*) ○, 'data' estimated by Jyotsna & Rao (1997) as explained in the text; black dashed line (3.60); black dotted line, (3.61), (*c*) ○, DEM data obtained from the present work, —, (3.40).

For the model of Henann & Kamrin (2013), the parameters μ_s, $\Delta\mu$ and I_0 are taken to be the same as those estimated earlier for the model of Barker *et al.* (2017). The value of A is set to 0.48 (Henann & Kamrin 2013). For the model of Dsouza & Nott (2020), $\mu_* = \sin\theta$ (Prakash & Rao 1988) where θ is the angle of internal friction at a critical state. It is assumed that $\theta = 25^\circ$, a typical value for glass beads. The value of ℓ in the model of Dsouza & Nott (2020) is estimated as discussed in § 4.5.

4. Results

4.1. *DEM*

We first consider the trends shown by the DEM, and then compare them with the model predictions. For smooth walls, the magnitude of the scaled vertical velocity $-u_y/\sqrt{gW}$, where g is the acceleration due to gravity and W is the half-width of the channel in the x-direction, decreases as x increases (see the symbols in figure 3). This is in accord with expectation and experimental observations that the walls retard the flow of the material. For a fixed value of $2\,W/d_p$, the flow is expected to become faster as the bulk solids fraction $\bar{\phi}$ decreases. Hence $-u_y$ increases. Similarly, as $2\,W/d_p$ increases, the confining effect of the walls decreases and hence the flow is faster. Rough walls retard the flow and hence the velocities are smaller in magnitude than for the smooth walls (the insets in figure 3). Even though it is often assumed that rough walls imply no slip, this is not true for the parameter values used here.

The thickness Δ of the shear layer is chosen as $W - x_*$, where $u_y(x_*) - u_y(W) = 0.95\,(u_y(0) - u_y(W))$. For smooth walls, the dimensionless thickness Δ/d_p is in the range 4–9 (the open black symbols in figure 4*a*). If Δ scales with d_p, Δ/d_p should be independent of W, but it appears to increase with W. Computations should be done over a larger range of W values to check whether this is a general trend. The main obstacle here is that the DEM calculations become very time consuming when the number of particles increases. As expected, rough walls lead to thicker shear layers (the filled black symbols in figure 4*a*). As $\bar{\phi}$ decreases, the thickness increases for both smooth and rough walls.

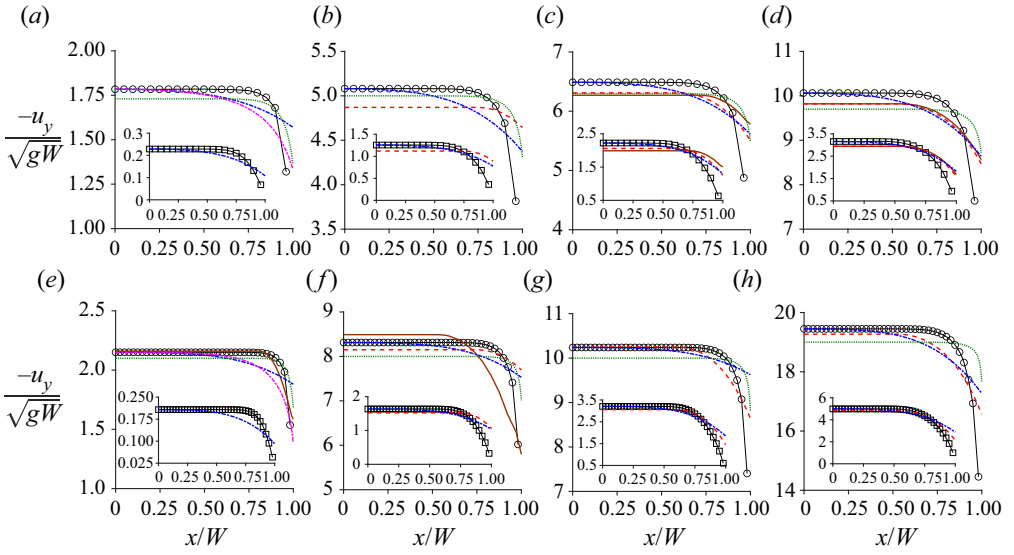

Figure 3. Variation of the scaled vertical velocity $-u_y/\sqrt{gW}$ with x/W for smooth (main figures) and rough (insets) walls, where g is the acceleration due to gravity, W is the half-width of the channel and x is the horizontal coordinate. The first row (a–d) and second row (e–h) correspond to $2W/d_p = 40$ and 80, respectively, where d_p is the particle diameter: $\bar{\phi} = 0.62$, (a,e); 0.61, (b,f); 0.60, (c,g); 0.59, (d,h). Here, $\bar{\phi}$ is the bulk solids fraction. The symbols correspond to the DEM results, and the curves to the predictions of the models: Barker *et al.* (2017) (brown solid line); Schaeffer *et al.* (2019) (red dashed line); Henann & Kamrin (2013) (green dotted line); Dsouza & Nott (2020) (magenta dash-dotted line – numerical solution, blue – approximate solution).

It is of interest to compare the mass flow rate $\dot{M}$ obtained from the DEM with that predicted by the correlation of Beverloo, Leniger & Van de Velde (1961) ($\dot{M}_b$). The latter has been deduced from data for flow through bins with circular exit slots, and can be modified as suggested by Nedderman *et al.* (1982) for rectangular exit slots. The solids fraction ϕ used in the correlation is taken as 0.6, which is within the range of $\bar{\phi}$ values used in the present work. The comparison of $\dot{M}$ with $\dot{M}_b$ is not strictly valid, as the actual bin has impermeable walls in the z-direction, whereas the present work is based on the use of periodic b.c.s in this direction. For smooth walls, $\dot{M}/\dot{M}_b$ is in the range 1–18 (figure 4c). Thus the DEM overestimates $\dot{M}$, probably because the bin width $2W$ and the slot width $\boldsymbol{D}$ are equal in the former case (figure 1b,c) but $2W > \boldsymbol{D}$ in the latter case (figure 1a). The discrepancy increases when $\bar{\phi}$ decreases, in keeping with the trends shown by the DEM for the scaled centreline velocity $-u_y(x = 0)/\sqrt{gW}$ (figure 3). (The mass flow rate $\dot{M}$ depends on u_y and ϕ, but the dependence on u_y is stronger as ϕ varies only slightly except close to the wall (figure 5).) For a fixed value of $\bar{\phi}$, $\dot{M}/\dot{M}_b$ increases as $2W/d_p$ increases. This is because $\dot{M}_b$ is independent of W but $\dot{M}$ increases as W increases.

For rough walls, $\dot{M}$ is lower than that for smooth walls (figure 4c). However, $\dot{M}_b$ corresponds to a situation where there is a core of rapidly flowing material near the exit slot, adjacent to static or quasistatic 'shoulders' of material. Thus the material flows through a channel with curved, rough walls, and there is no explicit dependence on wall roughness in the correlation of Beverloo *et al.* (1961). For $\bar{\phi} = 0.62$, $\dot{M}/\dot{M}_b < 1$, unlike the case for smooth walls. As mentioned earlier, there is no flow for $\bar{\phi} > 0.62$, and hence the material slows down considerably as this limit of $\bar{\phi}$ is approached. The effect may be more pronounced for rough walls, leading to $\dot{M}/\dot{M}_b < 1$.

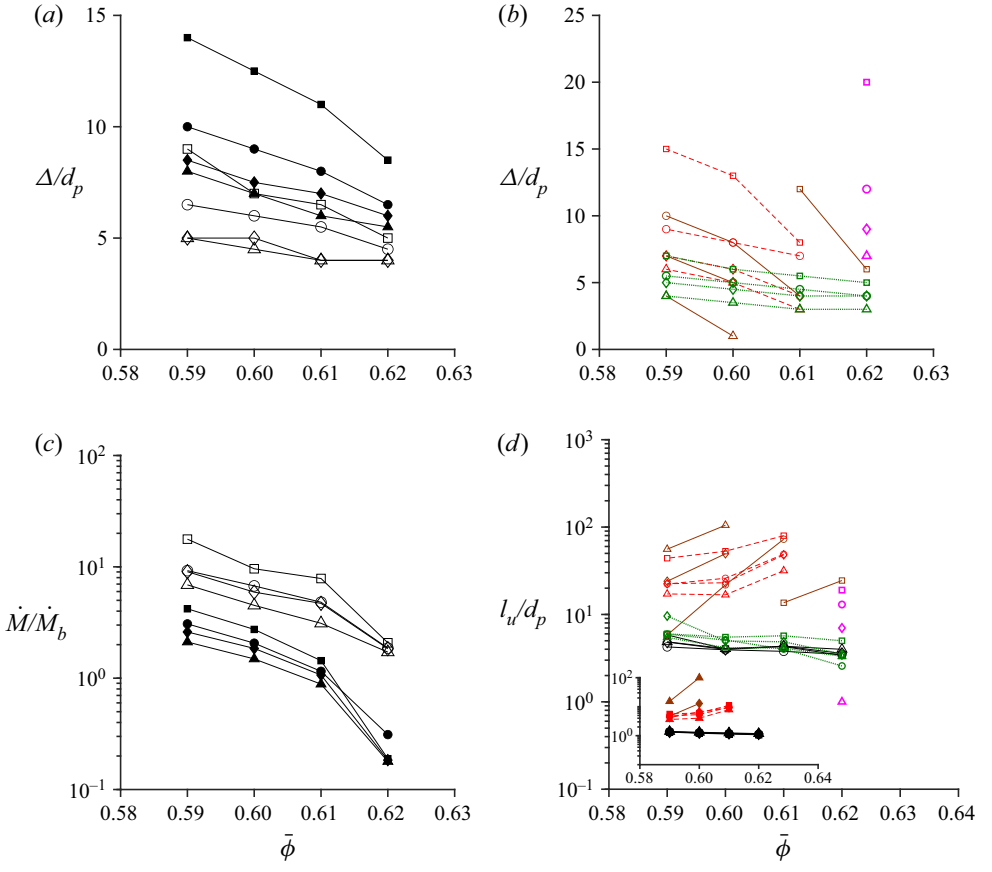

Figure 4. Variation of the dimensionless thickness of the shear layer Δ/d_p (*a*,*b*); (*a*) DEM results, (*b*) model results; mass flow rate $\dot{M}/\dot{M}_b$ (*c*) and slip length l_u/d_p (*d*) with $\bar{\phi}$: $2\,W/d_p = 30$ (△); 40 (◇); 50 (○); 80 (□). The open and filled symbols correspond to the smooth and rough walls, respectively, and the black symbols to the DEM results. The model predictions are shown by the coloured symbols and the curves joining them: Barker *et al.* (2017) (brown solid line); Schaeffer *et al.* (2019) (red dashed line); Henann & Kamrin (2013) (green dotted line); Dsouza & Nott (2020) (magenta – numerical solution).

In the actual bin, $\bar{\phi}$ is not within the control of the experimenter for a fixed slot width. As there is no exit slot in the present work, the magnitude of the centreline velocity $-u_y(x=0)$ is several multiples of $\sqrt{gW}$, where g is the acceleration due to gravity. Bhateja & Khakhar (2020) have simulated slow flow in a bin with slot widths in the range 6–8 d_p, and with $\boldsymbol{D}/(2\,W)$ in the range 0.2–0.27 (figure 1*a*); they obtained smaller centreline velocities ($\approx 0.13\sqrt{gW}$–$0.25\sqrt{gW}$). In their study, the periodic b.c. in the flow direction was relaxed, but particles leaving the bin were re-introduced at the top and allowed to fall from rest at random horizontal positions. The effect of the walls was removed by applying periodic b.c.s in the other two directions, and hence the properties varied in the flow direction only. Alternatively, the emptying of a bin can be examined. At some height between the free surface and the exit slot, a quasi-steady state may be expected to prevail for a time interval before the bin is fully empty. For example, the emptying of seeds from an axisymmetric bunker was studied by Danczyk *et al.* (2020) using experiments and DEM simulations.

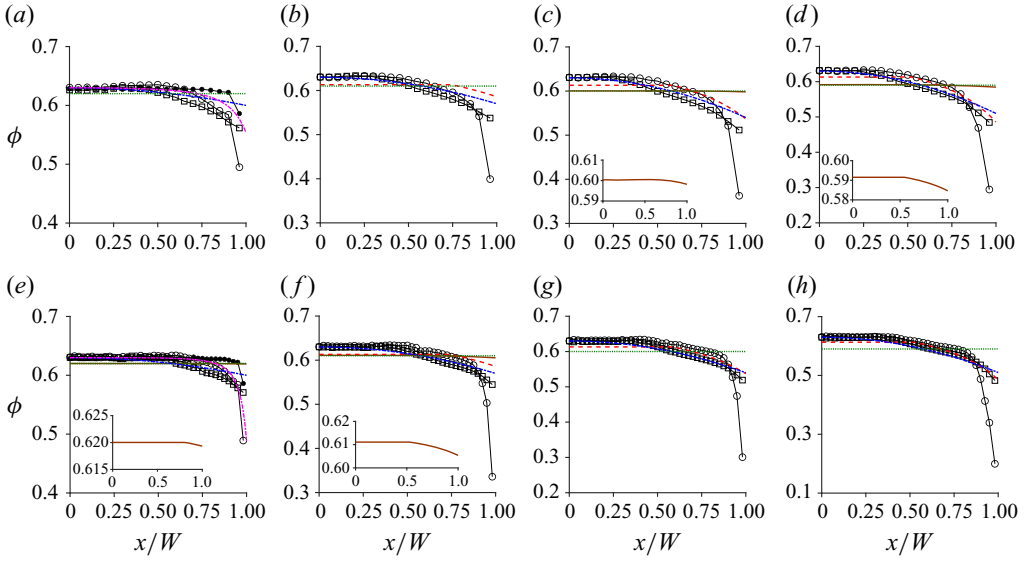

Figure 5. Variation of the solids fraction ϕ with x/W: $\bar{\phi} = 0.62$ (*a*,*e*); 0.61, (*b*,*f*); 0.60, (*c*,*g*); 0.59, (*d*,*h*). Panels (*a–d*) and (*e–h*) correspond to $2\,W/d_p = 40$ and 80, respectively. The symbols correspond to the DEM results for smooth (○) and rough (□) walls, and the curves to the model predictions of Barker *et al.* (2017) (brown solid line); Schaeffer *et al.* (2019) (red dashed line); Henann & Kamrin (2013) (green dotted line); Dsouza & Nott (2020) (magenta dash dot line – numerical solution, blue – approximate solution). The variation of ϕ in a static column is shown by black filled symbols in (*a*,*e*).

In the simulations, the velocity profile 'reached steady state flow after about 1 s. Steady flow continued until approximately 18 s, at which point all the seeds had drained from the hopper'. Some of these strategies will be examined in future work to permit a comparison with experiments.

The slip length l_u in (3.33) is evaluated in the DEM as $l_u/d_p = (u_y(x = W - 0.75\,d_p) - u_y(x = W - 2\,d_p))/(1.25\,d_p u_y(x = W - 0.75\,d_p))$, where $(x = W - 0.75\,d_p)$ and $(x = W - 2\,d_p)$ are the centres of two bins adjacent to the wall. The distance between the centres of these bins is $1.25\,d_p$. The slip length is approximately independent of W and $\bar{\phi}$ for both smooth and rough walls (figure 4*d*). This is an encouraging result, as it suggests that l_u may indeed be a material parameter that is related to the wall roughness. Further studies are needed to confirm this conjecture. The slip length is approximately 4 times higher for smooth walls than for rough walls. It may be expected that the magnitude of the velocity decreases and the magnitude of the velocity gradient increases as the wall roughness increases, leading to a lower value of l_u.

For the static column, the ϕ profile is approximately flat except near the wall, where it decreases (the black filled symbols in figure 5*a*,*e*). Because the material is sheared near the wall but not near the centre, the solids fraction ϕ is expected to be lower at the wall (figure 5). For smooth walls, there is a sharp decrease near the wall, and the values are less than ϕ_{min}. Thus frictional effects are expected to be small compared with collisional effects in this region. For a fixed value of $2\,W/d_p$, as $\bar{\phi}$ decreases, the ϕ profiles shift downward, except near the centre. This is expected as $\bar{\phi}$ represents the average value of ϕ. However, the value of $\phi(x = 0)$ is largely independent of the value of $\bar{\phi}$, for reasons that are not clear. For a fixed value of $\bar{\phi}$, the ϕ profiles are not affected much by changes in $2\,W/d_p$, except near the wall. For rough walls, the decrease is less pronounced, and the

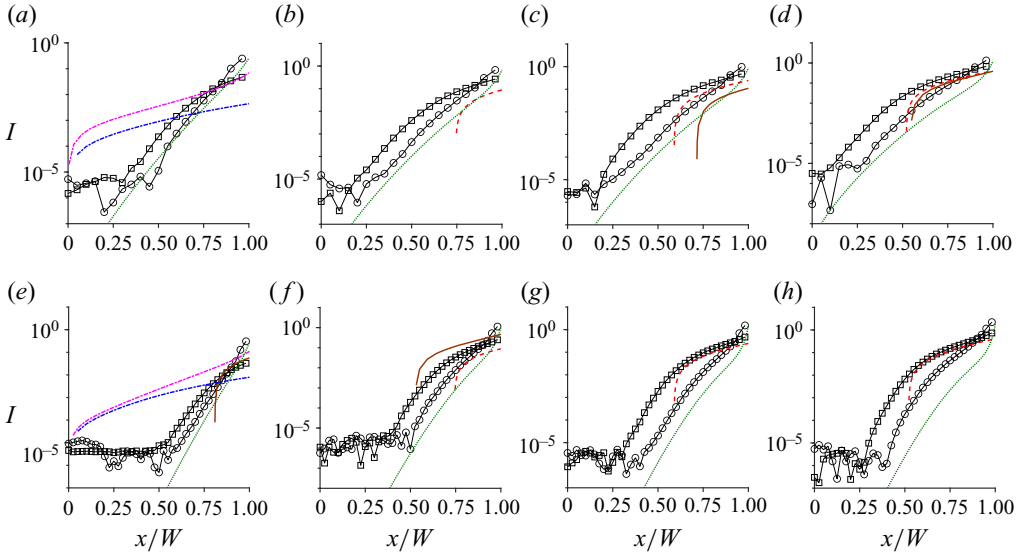

Figure 6. Variation of the inertial number I with x/W. The first row (*a–d*) and second row (*e–h*) correspond to $2\,W/d_p = 40$ and 80, respectively: $\bar{\phi} = 0.62$ (*a*,*e*); 0.61 (*b*,*f*); 0.60 (*c*,*g*); 0.59 (*d*,*h*). The symbols correspond to the DEM results for smooth (○) and rough (□) walls, and the curves to the model predictions of Barker *et al.* (2017) (brown solid line); Schaeffer *et al.* (2019) (red dashed line); Henann & Kamrin (2013) (green dotted line); Dsouza & Nott (2020) (magenta dash-dotted line – numerical solution, blue – approximate solution).

curves for smooth and rough walls cross near the wall. We do not have a simple qualitative explanation for this behaviour, even though it would be very desirable.

Consider the variation of the inertial number I, defined by (3.2). In the literature, the characteristic normal stress N is chosen as $N = p \equiv (\sigma_{xx} + \sigma_{yy} + \sigma_{zz})/3$, where p is the pressure. As mentioned in the previous section, two of the models do not provide estimates of σ_{zz}, and other two models do not predict normal stress differences. To facilitate comparison with these models, N is calculated as $N = \sigma_{xx}$. It is found that there is only a slight difference in the values of I calculated using p and σ_{xx} (not shown). The inertial number varies from very small values of order 10^{-5} (approximately zero) at the centre to large values of order 1 at the wall (figure 6). Thus the flow is quasistatic near the centre and inertial near the wall. The situation is unlike the case of steady flow down an inclined plane, where I is a constant and the velocity varies in the cross-stream direction (Pouliquen *et al.* 2006). Here, both I and u_y vary with x. For a fixed value of $2\,W/d_p$, I increases as the bulk solids fraction $\bar{\phi}$ decreases (figure 6). This is in accord with intuition, as inertial effects are expected to become more important in systems that are less dense. The value of I for rough walls is greater than that for smooth walls over most of the channel, probably because the shear rate is expected to be higher in the former case. However, close to the wall, the trend is reversed. As the width $2\,W/d_p$ increases, the confining effect of the walls decreases. Hence it may be expected that the flow will be faster, and the shear rate will be higher near the wall. This leads to a larger value of I. This is not a rigorous argument, but merely one based on intuition.

The y-component of the momentum balance shows that the shear stress τ varies linearly with x if ϕ is a constant. This condition holds in the plug region, but is violated in the shear layer. The DEM results show an approximately linear variation, with slight deviations apparent in the shear layer (figure 7*a*,*b*).

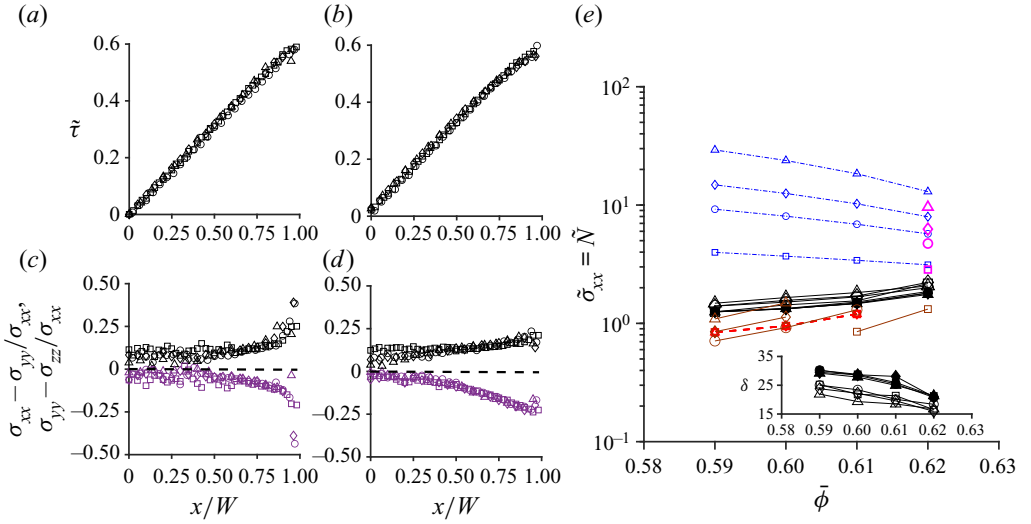

Figure 7. Variation of the scaled shear stress $\tilde{\tau} = \tau/(\rho_p g W)$ with x/W for smooth (a) and rough (b) walls. In (c,d), the markers above and below the horizontal dashed line correspond to the scaled first $(\sigma_{xx} - \sigma_{yy})/\sigma_{xx}$ and second $(\sigma_{yy} - \sigma_{zz})/\sigma_{xx}$ normal stress differences, respectively, for smooth (c) and rough (d) walls. The data shown in (a–d) represent the DEM results for $\bar{\phi} = 0.60$. (e) Variation of the scaled normal stress $\tilde{\sigma}_{xx} = \tilde{N} = \sigma/(\rho_p g W)$ with $\bar{\phi}$. Its inset shows the DEM results for the angle of wall friction δ (in degrees) (see (3.34)). In (a–e), $\triangle$, $\diamond$, $\circ$ and $\square$ are for $2\,W/d_p = 30$, 40, 50 and 80, respectively. In (e), the open and filled symbols correspond to smooth and rough walls, respectively, the black symbols to the DEM results, and the curves to the models predictions of Barker *et al.* (2017) (brown symbols solid line); Schaeffer *et al.* (2019) (red symbols dashed line); Dsouza & Nott (2020) (magenta symbols – numerical solution, blue symbols dash-dotted line – approximate solution).

For smooth walls, the scaled first normal stress difference $(\sigma_{xx} - \sigma_{yy})/\sigma_{xx}$ is positive, and varies from approximately 10 % at the centre to approximately 30 % near the wall (figure 7c). The scaled second normal stress difference $(\sigma_{yy} - \sigma_{zz})/\sigma_{xx}$ is largely negative, and is almost zero at the centre and approximately 30 % near the wall. Such differences do not appear to have been reported earlier for fully developed flow through a channel. As discussed later, they provide a stringent test of constitutive equations. Unfortunately, we do not have a simple physical explanation for their occurrence. Silbert *et al.* (2001) observed the normal stress difference of approximately 15 %–20 % in inclined chute flow, but they too did not provide a simple explanation. For rough walls, the trends are similar (figure 7d), except that the values are slightly smaller in magnitude near the wall.

Values of the scaled normal stress $\tilde{N} \equiv N/(\rho_p g, W)$ are of $O(1)$ for the DEM results (figure 7e). For a fixed value of $2\,W/d_p$, $\tilde{N}$ decreases as $\bar{\phi}$ decreases. The stress tensor is evaluated as the sum of two contributions, one arising from contacts (including collisions), and one arising from streaming (Silbert *et al.* 2001). Our calculations show that the latter is small compared with the former. Small changes in $\bar{\phi}$ cause much larger changes in $\tilde{N}$. For systems with high values of $\bar{\phi}$, this may be anticipated as the frictional or contact stresses are known to be sensitive to small changes in ϕ. Further, the material is expected to lose sustained contact with the wall as $\bar{\phi}$ decreases. Hence $\tilde{N}$ is likely to decrease. As mentioned by one of the referees, the stress depends on both the strength of the contact forces and the number of contacts. If the latter dominates, $\tilde{N}$ will decrease as $\bar{\phi}$ decreases. However, we do not have a convincing argument to prove this assertion at present. It is hoped that a more satisfactory argument may be advanced in the future. For a fixed value of $\bar{\phi}$, $\tilde{N}$ is

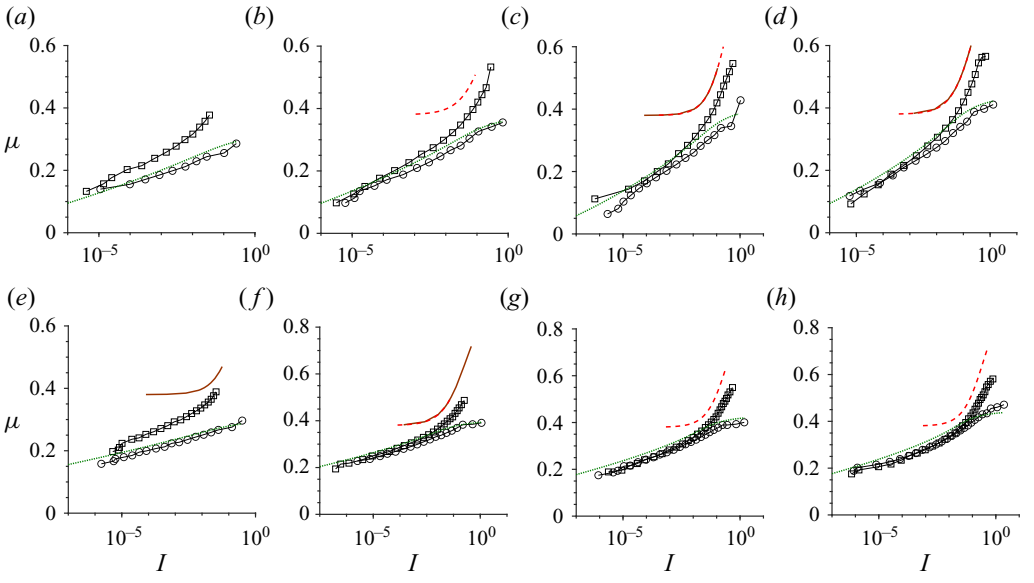

Figure 8. Variation of the friction coefficient μ with the inertial number I. The first row (*a–d*) and second row (*e–h*) correspond to $2\,W/d_p = 40$ and 80, respectively: (*a*,*e*), $\bar{\phi} = 0.62$; (*b*,*f*), $\bar{\phi} = 0.61$; (*c*,*g*), $\bar{\phi} = 0.60$; (*d*,*h*), $\bar{\phi} = 0.59$. The markers (○ – smooth walls, □ – rough walls) correspond to the DEM results and the curves to the model predictions of Barker *et al.* (2017) (brown solid line); Schaeffer *et al.* (2019) (red dashed line); Henann & Kamrin (2013) (green dotted line).

a very weak function of $2W/d_p$. Thus the scaling $\tilde{N} = N/(\rho_p g W)$ is reasonable but not exact. The normal stress for the smooth wall is approximately 12 %–20 % higher than that for the rough wall (figure 7*e*). Intuitively, as the angle of wall friction δ is expected to be higher for the rough wall, (3.35) explains the decrease of $\tilde{N}$ with the increase in wall roughness for a fixed value of $\bar{\phi}$.

The value of the angle of wall friction δ, calculated from (3.34) decreases by approximately 50 % of the larger value as $\bar{\phi}$ increases, for both smooth and rough walls (see the inset of figure 7*e*). For a fixed value of $\bar{\phi}$, δ is approximately 15 %–20 % higher for rough walls than for smooth walls. Compared with the slip b.c. (3.33), the wall friction b.c. (3.34) appears to be more robust. This issue merits further investigation.

As the shear rate and the shear stress increase with x/W and the normal stress N is a constant, both $\mu \equiv \tau/N$ and I increase, leading to the behaviour shown in figure 8. For very small values of I, μ appears to tend to a non-zero value. For intermediate values of I, the curves for smooth and rough walls are almost identical except for $\bar{\phi} = 0.62$. For large values of I, μ is larger for rough walls than for smooth walls (figure 8). As the curves for I (figure 6) intersect near the wall, the value of I in the wall region is lower for the rough wall . Hence, for a fixed value of I, the corresponding value of x/W is larger for the rough wall, leading to a larger value of τ. As the normal stress N is also smaller for the rough wall (figure 7*e*), μ is higher near the wall.

As I increases, the shear rate increases. Hence the material is expected to dilate more leading to a lower value of ϕ, or a higher value of $\phi_{drp} - \phi$ (figure 9). Except for $\bar{\phi} = 0.62$, the results for smooth and rough walls almost coincide, indicating that ϕ vs I relation is independent of the wall roughness. For $\bar{\phi} = 0.62$, ϕ is slightly lower for rough walls.

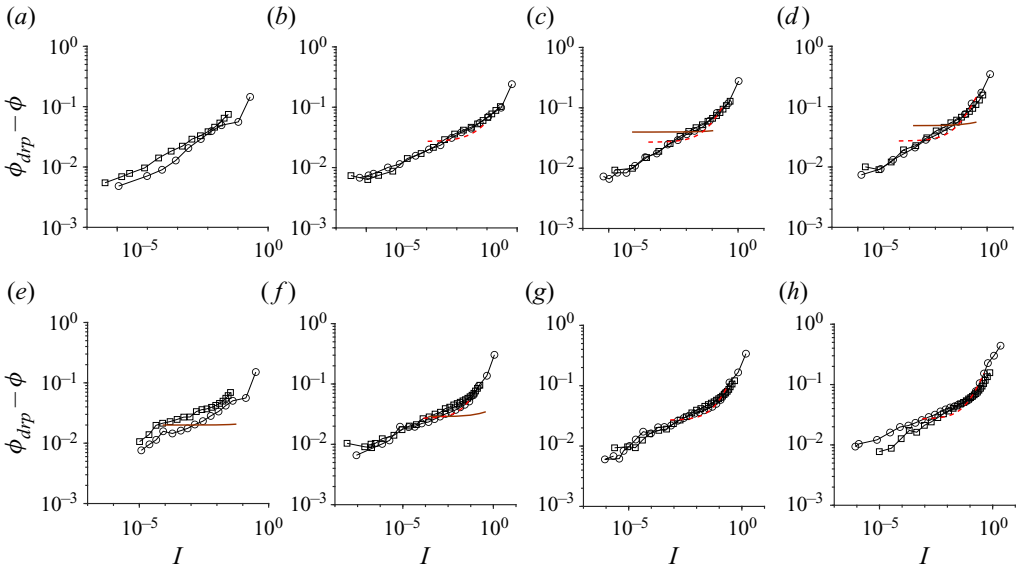

Figure 9. Variation of $\phi_{drp} - \phi$ with I. The first row (*a–d*) and second row (*e–h*) correspond to $2\,W/d_p = 40$ and 80, respectively: (*a*,*e*), $\bar{\phi} = 0.62$; (*b*,*f*), $\bar{\phi} = 0.61$; (*c*,*g*), $\bar{\phi} = 0.60$; (*d*,*h*), $\bar{\phi} = 0.59$. The markers (○ – smooth walls, □ – rough walls) correspond to the DEM results; Barker *et al.* (2017) (brown solid line); Schaeffer *et al.* (2019) (red dashed line).

For $2\,W/d_p = 80$, there are two distinct regimes, except for $\bar{\phi} = 0.62$, (i) where $\phi_{drp} - \phi$ increases gradually with I, and (ii) where $\phi_{drp} - \phi$ increases more rapidly for $I > 10^{-1}$.

4.2. *Barker et al. (2017)*

For reasons explained in § 4.2.1, this model could not be solved for the entire range of parameter values used here. Using (3.23), (3.25), (3.27) and (3.31), ϕ, I and N can be obtained independently of the wall roughness. This result is a consequence of matching $\bar{\phi}$ to the DEM results, and not using the alternative b.c. (3.34). Hence the velocity gradient (3.30) is the same for both smooth and rough walls, and the velocity profile corresponds to a shift along the velocity axis when the wall roughness changes. Thus the form of the velocity profile in unaffected by the wall roughness, as shown in figure 3(*c*,*d*) (the brown curves). The same conclusion holds for the model of Schaeffer *et al.* (2019).

For $2\,W/d_p = 40$, the magnitude of the scaled velocity is qualitatively similar to the DEM results (the brown curves in figure 3*c*,*d*). The values are underestimated near the centre and overestimated near the wall for both smooth and rough walls.

For $2\,W/d_p = 80$ and $\bar{\phi} = 0.62$, the profile agrees fairly well with the DEM results for smooth walls (the brown curve in figure 3*e*). However, the values are overestimated near the centre and underestimated near the wall for $\bar{\phi} = 0.61$ and smooth walls, unlike the case for $2\,W/d_p = 40$ (the brown curve in figure 3*f*). For rough walls, the scaled velocity changes sign near the wall because of the shift, and hence leads to unrealistic profiles (not shown in figure 3*e*,*f*).

The scaled thickness of the shear layer Δ/d_p varies with $\bar{\phi}$ and $2\,W/d_p$ like the DEM results (the brown symbols in figure 4*b*). It is of the same order of magnitude, but the range is larger than the latter. For reasons explained earlier, this model predicts that Δ/d_p is independent of the wall roughness, in contrast to the DEM results.

The values of the slip length l_u calculated from (3.33) vary widely (the brown symbols in figure 4*d*). In some cases, they exceed the half-width of the channel. Thus this b.c. is not reasonable for this model. Conversely, if l_u is treated as a material parameter, the predicted mass flow rates will differ significantly from the DEM results.

The solids fraction profiles are approximately flat, as shown by the insets of figure 5(*c–f*) (the brown curves). It behaves like an incompressible model, at least in the present problem, and hence does not match the DEM results well. As discussed earlier, the profiles are independent of the wall roughness for a fixed value of $\bar{\phi}$.

The vertical asymptotes in the I profiles correspond to the boundary between the plug and the shear layers (the brown curves in figure 6*c–f*), whereas the DEM results show a more gradual variation. The profiles agree reasonably well with the latter near the wall.

The scaled shear stress $\tilde{\tau}$ almost coincides with the DEM results for all the models, and hence the profiles are not shown. The first normal stress difference $\sigma_{xx} - \sigma_{yy}$ is zero, and the second normal stress difference $\sigma_{yy} - \sigma_{zz}$ cannot be evaluated as σ_{zz} is unknown. This is at variance with the DEM results, particularly near the wall (figure 7*c*,*d*). The scaled normal stress $\tilde{N} = N/(\rho_p g W)$ underestimates the DEM results, and is independent of wall roughness as mentioned earlier (the brown symbols in figure 7*e*). Unlike the latter, $\tilde{N}$ varies more strongly with $2\,W/d_p$ and $\bar{\phi}$.

Hence the angle of wall friction δ cannot be treated as a material parameter (see (3.35)). Further, as $\tilde{N}$ is independent of wall roughness, the model predicts that δ is also independent of the wall roughness, contrary to expectation. This problem arises because $\bar{\phi}$ has been matched to the DEM value. On the other hand, if δ is determined from independent experiments, then the predicted value of $\bar{\phi}$ for a fixed value of $2\,W/d_p$ may not match the value used to generate the DEM results.

From (3.26), as $I \to 0$, $\mu \to \mu_s = 0.38$, which is much larger than the DEM results (the brown curves in figure 8*c–f*). At large values of I, the trends are similar to the DEM results for rough walls, but the values of μ are overestimated. For smooth walls, the latter show a different curvature. Thus a single function $\mu(I)$ cannot fit data for both smooth and rough walls. The brown curves in figure 8(*c–f*) are obtained by fitting (3.26) to the DEM results of Chialvo *et al.* (2012) for homogeneous shear between parallel plates (figure 2*a*). As this function does not fit our DEM results well, it follows that $\mu(I)$ is not a true constitutive equation, but one that depends on the geometry. As ϕ does not vary much with x/W (the insets in figure 5*c–f*), plots of ϕ vs I are effectively horizontal lines, and hence they do not capture the variation shown by the DEM results (the brown curves in figure 9).

4.2.1. *Reasons for the lack of solutions for some parameter values*

Introducing the dimensionless quantities $\tilde{x}_p \equiv x_p/W$ and $\tilde{N} \equiv N/(\rho_p g W)$, (3.29) reduces to $\tilde{x}_p = (\mu_s \tilde{N})/\phi_p$. As $\tilde{x}_p \leqslant 1$, we have

$$\mu_s \tilde{N} \leqslant \phi_p. \tag{4.1}$$

As $\beta(I \to 0) = 2\,\mu_s$, (3.27) implies that

$$\phi_p = \frac{\mu_s \tilde{\Lambda} \phi_{min} + \tilde{N} \phi_{max}}{\mu_s \tilde{\Lambda} + \tilde{N}}, \tag{4.2}$$

where $\tilde{\Lambda} \equiv \Lambda/(\rho_p g W)$. Using (4.1) and (4.2), we obtain

$$\mu_s \tilde{N}^2 + (\mu_s^2 \tilde{\Lambda} - \phi_{max})\tilde{N} - \mu_s \tilde{\Lambda} \phi_{min} \leqslant 0. \tag{4.3}$$

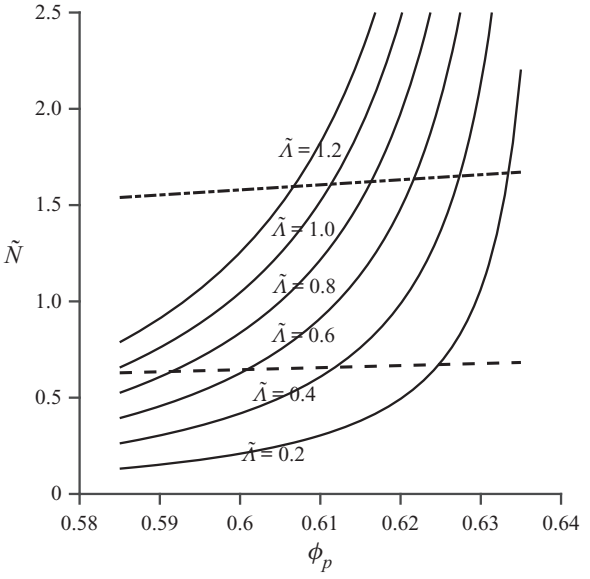

Figure 10. Variation of the dimensionless normal stress $\tilde{N}$ with the solids fraction ϕ_p in the plug layer for the model of Barker *et al.* (2017): solid curves, plots of (4.2) for specified values of $\tilde{\Lambda} = \Lambda/(\rho_p g W)$, where ρ_p is the particle density, g is the acceleration due to gravity and W is the half-width of the channel in the x-direction; upper dash-dot line, equality in (4.1); lower dashed line, equality in (4.6).

For (4.3) to hold, $\tilde{N}$ must be less than a critical value $\tilde{N}_c$, which is the positive root obtained by equating the left-hand side of (4.3) to zero. For a chosen value of $\tilde{\Lambda}$, the root corresponds to the point of intersection of the curve (4.2) and the line given by equality in (4.1) in the ϕ_p–$\tilde{N}$ plane (figure 10). For a value of $2\,W/d_p$, or $\tilde{\Lambda}$, if the curve (4.2) corresponding to that $\tilde{\Lambda}$ crosses the line (4.1) at a $\phi_p = \phi_u$, the model cannot be solved for $\bar{\phi} > \phi_u$.

An approximate solution provides an additional insight. As seen from our DEM results, the model predicts a very small variation of ϕ (the insets in figure 5*c–f*). Treating ϕ as a constant ($=\phi_p$), and using (3.25) and (3.26), the second of (3.23) can be integrated to obtain

$$\frac{I}{I_0 + I} = \frac{\phi_p}{\tilde{N}\Delta\mu}(\tilde{x} - \tilde{x}_p), \tag{4.4}$$

where $\tilde{x} \equiv x/W$ and $\tilde{x}_p \equiv x_p/W$. Simplifying, we obtain

$$I = \frac{I_0(\tilde{x} - \tilde{x}_p)}{\left(\dfrac{\tilde{N}\mu_d}{\phi_p} - \tilde{x}\right)}; \quad \mu_d \equiv \mu_s + \Delta\mu. \tag{4.5a,b}$$

Equation (4.5*a*,*b*) shows that $I \to \infty$ as $\tilde{x}$ increases if

$$\frac{\tilde{N}\mu_d}{\phi_p} \leqslant 1. \tag{4.6}$$

For a chosen value of $\tilde{\Lambda}$, the limiting condition corresponds to the intersection of the curve (4.2) with the line given by the equality in (4.6) (figure 10). This gives a limiting value of

$\phi_p = \phi_l$ such that there is no solution for $\bar{\phi} < \phi_l$. Thus the model cannot be solved for both small and large values of $\bar{\phi}$, but the limits depend on the value of $\tilde{\Lambda}$. The lower limit should be used with care as it is based on an approximate solution.

For typical values of a particle density $\rho_p = 2650$ kg m^{-3}, $\Lambda = 555$ N m^{-2}, a particle diameter $d_p = 1$ mm and $2\,W/d_p = 30$, 40, 50 and 80, the values of $\tilde{\Lambda} = \Lambda/(\rho_p g W)$ are 1.4, 1.1, 0.8 and 0.5, respectively. For these values of $\tilde{\Lambda}$, figure 10 shows that solutions can be obtained for $\bar{\phi} = (0.6, 0.59)$ for $2\,W/d_p = 30$ and 40, (0.61, 0.6, 0.59) for $2\,W/d_p = 50$ and (0.62, 0.61) for $2\,W/d_p = 80$.

4.3. *Schaeffer et al. (2019)*

As $\bar{\phi}$ is matched to the DEM results and $\phi_c = 0.613$ in (3.40), a solution could not be obtained for $\bar{\phi} = 0.62$. As $\phi(x = 0) \approx 0.63$ for the DEM results and $\phi(x = 0) \leqslant \phi_c$ for the model, we expect the predictions to overestimate ϕ near the wall for $\bar{\phi} \leqslant 0.61$ (the red curves in figure 5). The scaled velocity profiles are qualitatively similar to the DEM results, except that the values are higher near the wall and lower near the centre (the red curves in figure 3). This holds for both smooth and rough walls. The scaled thickness of the shear layer Δ/d_p overestimates the DEM results for most of the parameter values (the red symbols in figure 4*b*), but is of the same order of magnitude. It varies with $2\,W/d_p$ and $\bar{\phi}$, but does not vary with the wall roughness, similar to that of Barker *et al.* (2017). The range of l_u/d_p values is comparable to that of Barker *et al.* (2017) (the red symbols in figure 4*d*). As in the case of the latter, l_u is not a material parameter.

The ϕ profiles (the red curves in figure 5) are better than the flat profiles predicted by Barker *et al.* (2017). However, there is no improvement in the profiles of I, which are similar to those of Barker *et al.* (2017), except near the wall (the red curves in figure 6). For a fixed value of $\bar{\phi}$, the I profiles are independent of $2\,W/d_p$ unlike the profiles of Barker *et al.* (2017). This is because the right-hand side of (3.41) involves the ratio of x/W to the scaled normal stress $\tilde{N} = N/(\rho_p g W)$, and W does not occur explicitly. Hence ϕ is independent of $2\,W/d_p$ (see (3.40)), leading to a similar behaviour for $\tilde{N}$ (the red symbols in figure 7*e*). Equation (3.35) shows that δ is also independent of $2\,W/d_p$, and varies only with $\bar{\phi}$. The values $\tilde{N}$ are underestimated. The first normal stress difference is zero, and the second normal stress difference is undetermined. As explained in § 4.2, the profiles of ϕ, I, and $\tilde{N}$ are unaffected by the wall roughness, and hence the remarks about the use of the friction b.c. (3.35) apply here also.

The profiles of μ vs I are identical to those of Barker *et al.* (2017), as (3.26) has been used in both cases (the red curves in figure 8). For I in the range 0.002–0.2, (3.40) has been fitted to the DEM results. Hence the agreement is good (the red curves in figure 9). For smaller values of I, deviations are apparent.

4.4. *Henann & Kamrin (2013)*

For smooth walls, the scaled velocity profiles are qualitatively similar to those for the DEM results (the green curves in figure 3), but the values are underestimated near the centre and overestimated near the wall. For rough walls, the solution could not be obtained as discussed in § 4.4.1. For smooth walls, the scaled thickness of the shear layer is comparable to the DEM results (the green symbols in figure 4*b*).

The value of the slip length l_u is approximately independent of $\bar{\phi}$ and $2\,W/d_p$, and comparable to the DEM results (the green symbols in figure 4*d*). Hence it appears that the slip velocity b.c. (3.33) can be used for this model, with l_u as a material parameter.

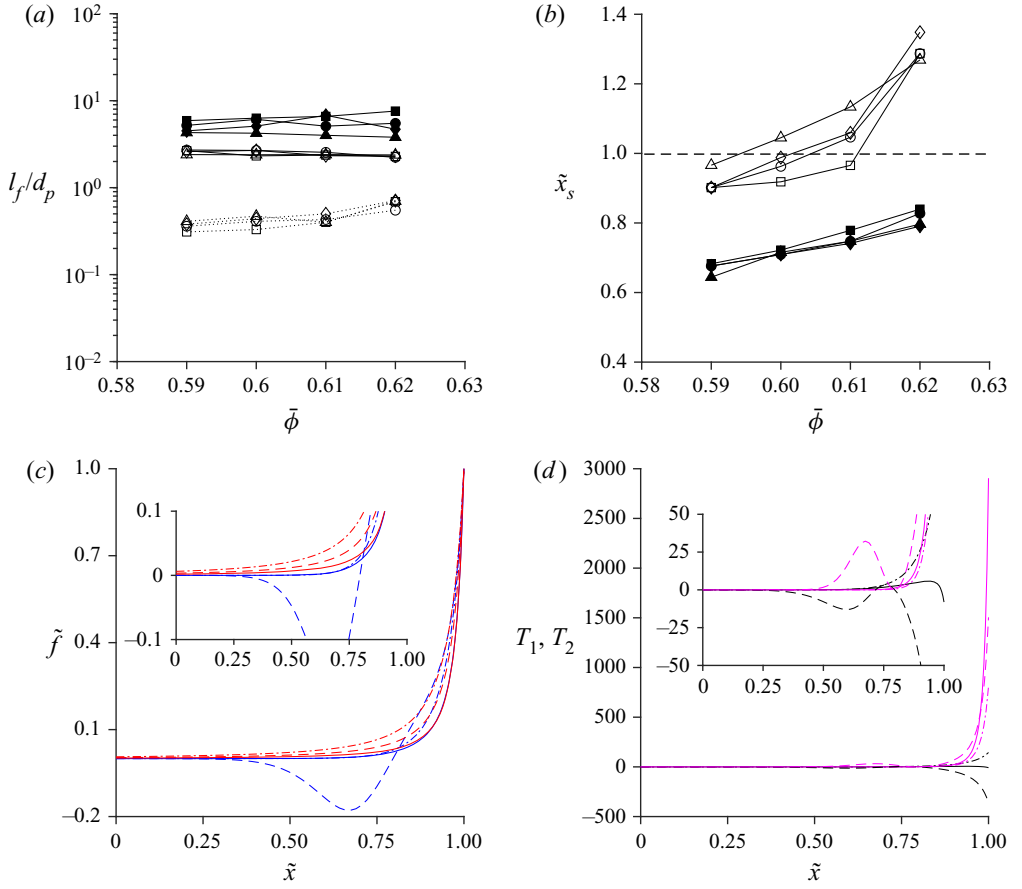

Figure 11. Variation of l_f (*a*) and $\tilde{x}_s = \mu_s \tilde{N}/\phi_p$ (*b*) with $\bar{\phi}, \tilde{f} = f/f_w$ (*c*) and T_1 and T_2 (*d*) with $\tilde{x} = x/W$ for the model of Henann & Kamrin (2013). Here, l_f is calculated from (3.58), T_1 and T_2 are defined by (4.9*a*,*b*). The value of $\tilde{N}$ is matched to the DEM results. In (*a*,*b*), open and filled symbols correspond to smooth and rough walls, and △, ◇, ○, and □ are for $2\,W/d_p = 30$, 40, 50 and 80, respectively. In (*a*), the solid lines correspond to the DEM results, and the dotted lines to the model predictions. In (*c*,*d*), $2\,W/d_p = 40$; black dash-dotted line, $\bar{\phi} = 0.62$ (smooth wall, $\tilde{x}_s > 1$); black solid line, $\bar{\phi} = 0.6$ (smooth wall, $\tilde{x}_s$ slightly < 1); black dashed line, $\bar{\phi} = 0.6$ (rough wall, $\tilde{x}_s$ much < 1). The numerical (blue) and approximate (red) solutions for $\tilde{f}$ are shown in (*c*). Using the numerical solution, the profiles of T_1 (black) and T_2 (magenta) are shown in (*d*).

The slip length for the fluidity l_f is calculated using (3.58), and is shown in figure 11(*a*). The DEM results of l_f for smooth walls do not vary with $2\,W/d_p$ and $\bar{\phi}$, which is not true for rough walls. For smooth walls, the value of l_f obtained from the model is much smaller than that for the DEM results, and shows a very weak dependence on $2\,W/d_p$ and $\bar{\phi}$. Thus (3.58) can possibly be used as a b.c., but the discrepancy in the l_f values shown in figure 11(*a*) suggests that it may not give good predictions of various quantities.

As ϕ is assumed to be a constant, the profiles are flat, in contrast to the DEM results (the green curves in figure 5). The variation of I with x/W is predicted fairly well by the model (the green curves in figure 6). The normal stress differences are zero (see (3.44)), in contrast to the DEM results. The scaled normal stress $\tilde{N}$ has been matched to the DEM values, and hence there is no discrepancy in the values of $\tilde{N}$ and δ. Conversely, if the value δ is taken from independent experiments, the predicted value of $\tilde{N}$ may not match the DEM

results. For smooth walls, μ vs I profiles are predicted much better than the other models (the green curves in figure 8). In particular, the change in curvature of the profiles near the wall for some of the parameter values is captured by the model. Solutions could not be obtained for some parameter values (e.g. for rough walls), for reasons discussed below.

4.4.1. *Reasons for the lack of solutions*

Introducing the dimensionless variables $\tilde{x} = x/W$, $\tilde{W} = W/d_p$, $\tilde{u}_y = u_y/\sqrt{gW}$, $\tilde{N} = N/(\rho_p g W)$, $\tilde{f} = f/f_w$, $\tilde{f}_w = f_w/\sqrt{g/W}$, where $f_w = f(x = W)$, and substituting μ from (3.52), (3.53) can be rewritten as

$$\frac{\mathrm{d}^2\tilde{f}}{\mathrm{d}\tilde{x}^2} = \frac{\Delta\mu}{A^2}\left(\frac{\tilde{x}_s - \tilde{x}}{\tilde{x}_d - \tilde{x}}\right)\tilde{W}^2\tilde{f} + \frac{\Delta\mu}{I_0 A^2}\frac{\phi_p}{\tilde{N}^{3/2}}\tilde{W}\tilde{f}_w\tilde{x}\tilde{f}^2, \tag{4.7}$$

or

$$\frac{\mathrm{d}^2\tilde{f}}{\mathrm{d}\tilde{x}^2} = T_1 + T_2, \tag{4.8}$$

where $\tilde{x}_s \equiv \mu_s\tilde{N}/\phi_p$ and $\tilde{x}_d \equiv (\mu_s + \Delta\mu)\tilde{N}/\phi_p$, and

$$T_1 \equiv \frac{\Delta\mu}{A^2}\left(\frac{\tilde{x}_s - \tilde{x}}{\tilde{x}_d - \tilde{x}}\right)\tilde{W}^2\tilde{f}; \quad T_2 \equiv \frac{\Delta\mu}{I_0 A^2}\frac{\phi_p}{\tilde{N}^{3/2}}\tilde{W}\tilde{f}_w\tilde{x}\tilde{f}^2. \tag{4.9a,b}$$

The values of μ_s and $\Delta\mu$ are such that $\tilde{x}_d > \tilde{x}_s$ and $\tilde{x}_d > 1$ for the ranges of $\tilde{N}$ and $\phi_p(= \bar{\phi})$ used here. However, $\tilde{x}_s$ may be > 1 for some cases (figure 11*b*). If $\tilde{x}_s > 1$, the right-hand side of (4.7) is non-negative. Using the b.c. (3.56), if $\tilde{f}(\tilde{x} = 0) > 0$, then (4.7) implies that $\tilde{f}$ increases monotonically throughout the domain. Hence a solution can be obtained that matches the b.c. (3.57) for smooth walls (the blue dash-dot curve in figure 11*c*).

If $\tilde{x}_s$ is slightly <1, T_1 is <0 near the wall, whereas T_2 is >0 (see (4.9*a*,*b*)). If the latter dominates, a solution can be obtained (the solid blue curve in figure 11*c*). If $\tilde{x}_s$ is much <1, T_1 is <0 for $\tilde{x}_s < \tilde{x} \leqslant 1$, and may dominate T_2 in magnitude. Hence the right-hand side of (4.7) may be negative for some values of $\tilde{x}$. This causes the slope $\mathrm{d}\tilde{f}/\mathrm{d}x$ to decrease. If the slope decreases, $\tilde{f}$ may eventually become < 0, as in the case of the blue dashed curve in figure 11(*c*). This is an unrealistic result as (3.45) implies that $\tilde{f}$ must be $\geqslant 0$. For rough walls, $\tilde{x}_s$ is significantly <1 (figure 11*b*), and hence a realistic solution could not be obtained.

4.4.2. *An approximate solution by the method of matched asymptotic expansion*

An insight into the behaviour of solutions to (4.7) may be obtained by omitting T_2 as discussed below, even though the numerical solution shows that $|T_1| \ll T_2$ near the wall (figure 11*d*). Introducing a small parameter $\varepsilon = 1/\tilde{W} = d_p/W$, $\tilde{f}$ may be expanded in powers of ε as

$$\tilde{f} = \tilde{f}_0(\tilde{x}) + \varepsilon\tilde{f}_1(\tilde{x}) + \varepsilon^2\tilde{f}_2(\tilde{x}) + \ldots. \tag{4.10}$$

Substituting (4.10) in (4.7), omitting T_2 and matching the terms of $O(\varepsilon^0)$, we obtain $\tilde{f}_0 = 0$. This does not satisfy the b.c. (3.57) at $\tilde{x} = 1$. Regarding this as the outer solution $\tilde{f}_{outer} = 0$ which is not valid near the wall, we seek an inner solution $\tilde{f}_{inner}$ by introducing a new

coordinate

$$X = (1 - \tilde{x})/\varepsilon. \tag{4.11}$$

Expanding $\tilde{f} = \tilde{f}_{inner} \equiv F$ in powers of ε, we obtain

$$F = F_0(X) + \varepsilon F_1(X) + \varepsilon^2 F_2(X) + \ldots. \tag{4.12}$$

Substituting (4.11) and (4.12) in (4.7), we obtain

$$\frac{\mathrm{d}^2 F}{\mathrm{d}X^2} = \frac{\Delta\mu}{A^2}\,\frac{\tilde{x}_s - (1 - \varepsilon X)}{\tilde{x}_d - (1 - \varepsilon X)}\,F. \tag{4.13}$$

The b.c.s required to solve (4.13) are $F(X = 0) = 1$ and $F \to \tilde{f}_{outer} = 0$ as $X \to \infty$. Substituting (4.12) in (4.13), and matching the terms of $O(\varepsilon^0)$, we obtain

$$\frac{\mathrm{d}^2 F_0}{\mathrm{d}X^2} = m^2 F_0, \tag{4.14}$$

where $m^2 = (\Delta\mu/A^2)((\tilde{x}_s - 1)/(\tilde{x}_d - 1))$, and the leading-order terms in the b.c. are $F_0(X = 0) = 1$ and $F_0 \to \tilde{f}_{outer}$ as $X \to \infty$.

Case 1: for $\tilde{x}_s > 1$, m^2 is > 0 and the inner solution is

$$\tilde{f}_{inner} = F = F_0 + O(\varepsilon) = \exp(-mX) + O(\varepsilon) = \exp\left(-\frac{m}{\varepsilon}(1 - \tilde{x})\right) + O(\varepsilon), \tag{4.15}$$

which ensures the solution $\tilde{f}$ is $\geqslant 0$ in the whole domain. The exponentially decaying trend of (4.15) from the wall towards the centre agrees qualitatively with the numerical results (the blue dash-dot curve and the blue solid curve in figure 11*c*).

Case 2: for $\tilde{x}_s < 1$, m^2 is < 0 and the inner solution is

$$\tilde{f}_{inner} = F(X) = F_0(X) + O(\varepsilon) = c_1 \cos(mX) + c_2 \sin(mX) + O(\varepsilon), \tag{4.16}$$

where c_1 and c_2 are constants. Using the b.c. $F_0(X = 0) = 1$, $c_1 = 1$. The b.c. $F_0 \to \tilde{f}_{outer}$ as $X \to \infty$ cannot be satisfied. Hence the solution (4.16) does not ensure $\tilde{f} \geqslant 0$ in the whole domain for the instances $\tilde{x}_s < 1$.

The above argument very crudely suggests that there is a possibility of obtaining a solution with $\tilde{f} < 0$ in a part of the domain if $|T_1| > T_2$. The numerical solution shows that T_2 is $\gg |T_1|$ near the wall, although both the terms are comparable in a zone far from the wall (figure 11*d*). This leads us to seek an approximate solution by omitting T_1.

Introducing a small parameter $\epsilon_* = 1/(\tilde{W}\tilde{f}_w)^{1/2}$ (the DEM results show that $\tilde{f}_w$ is of the same order as $\tilde{W}$), (4.7) can be rewritten as

$$\frac{\mathrm{d}^2\tilde{f}}{\mathrm{d}\tilde{x}^2} = \epsilon_*^2 \frac{\Delta\mu}{I_0 A^2}\,\frac{\phi_p}{\tilde{N}^{3/2}}\,\tilde{x}\tilde{f}^2. \tag{4.17}$$

Expanding $\tilde{f}$ in powers of ϵ_*

$$\tilde{f} = \tilde{f}_0 + \epsilon_*\tilde{f}_1 + \epsilon_*^2\tilde{f}_2 + \ldots. \tag{4.18}$$

Substituting (4.18) in (4.17), and matching the terms of $O(\epsilon_*^0)$, we obtain

$$\tilde{f}_0 = 0. \tag{4.19}$$

The solution (4.19) satisfies the b.c. $\mathrm{d}\tilde{f}/\mathrm{d}\tilde{x}(\tilde{x} = 0) = 0$, but not the b.c. $\tilde{f}(\tilde{x} = 1) = 1$. Hence we regard (4.19) as the outer solution $\tilde{f}_{outer}$.

To obtain the inner solution, let

$$\chi = \frac{1-\tilde{x}}{\epsilon_*}. \tag{4.20}$$

Expanding $\tilde{f} = \tilde{f}_{inner} \equiv \varphi$ in powers of ϵ_*, we obtain

$$\varphi = \varphi_0(\chi) + \epsilon_*\varphi_1(\chi) + \epsilon_*^2\varphi_2(\chi) + \ldots. \tag{4.21}$$

Substituting (4.21) in (4.17), we obtain

$$\frac{\mathrm{d}^2\varphi}{\mathrm{d}\chi^2} = \frac{\Delta\mu}{I_0A^2}\frac{\phi_p}{\tilde{N}^{3/2}}(1-\epsilon_*\chi)\varphi^2. \tag{4.22}$$

The b.c.s for (4.22) are $\varphi(\chi=0)=1$ and $\varphi \to \tilde{f}_{outer} = 0$ as $\chi \to \infty$. Substituting (4.21) in (4.22), and matching the terms of $O(\epsilon_*^0)$, we obtain

$$\frac{\mathrm{d}^2\varphi_0}{\mathrm{d}\chi^2} = \alpha\varphi_0^2, \tag{4.23}$$

where $\alpha = (\Delta\mu\phi_p)/(I_0A^2\tilde{N}^{3/2})$. Multiplying both sides of (4.23) by $\mathrm{d}\varphi_0/\mathrm{d}\chi$, and using the b.c.s $\varphi_0(\chi=1)=1$ and $\varphi_0 \to 0$ at $\chi \to \infty$, the inner solution is given by (Zaitsev & Polyanin 2002)

$$\tilde{f}_{inner} = \varphi = \frac{1}{\left(\sqrt{\frac{\alpha}{6}}\chi + 1\right)^2} + O(\epsilon_*). \tag{4.24}$$

The approximate solution (the red curves in figure 11*c*) agrees reasonably well with the numerical solution (the blue curves), except when the fluidity is negative.

4.4.3. *Use of $\phi = \phi(I)$ to improve the model*

To permit variation of ϕ with x, we assume that $\phi = \phi(I)$, and use the form (3.40). Equations (3.30), (3.50*a*,*b*) and (3.53) are solved using the b.c.s (3.56) and (3.57). As in the other models, $\bar{\phi}$ and $\dot{M}$ are matched to the DEM results. For $\bar{\phi} = 0.61$, the ϕ profiles (the blue and red solid curves in figure 12*b*) agree better with the DEM results than the incompressible model (the dashed line). Because $\phi(x=0) = \phi_c = 0.613$ at the centre, which is slightly $> \phi_p = \bar{\phi}$ for the incompressible model, we expect the scaled velocity to be smaller near the centre (the blue and red solid curves in figure 12*a*). The profiles of I for both the models are qualitatively similar (figure 12*c*). These remarks also apply to the case $\bar{\phi} = 0.60$ (figure 12*d–f*).

4.5. *Dsouza & Nott (2020)*

The value of the parameter ℓ is estimated by minimizing the root mean square error N_{rms} between the normal stresses N_{dem} and N_{model}, with

$$N_{rms} \equiv \sqrt{\frac{1}{n_p}\sum_{i=1}^{n_p}\left(\frac{N_{model}-N_{dem}}{N_{dem}}\right)^2}, \tag{4.25}$$

where n_p is the number of bins used for the DEM. For the models, $N_{model} = \sigma_{xx}$ is independent of x, but N_{dem} varies slightly. Here, N_{rms} increases with ℓ/d_p (figure 13*a*),

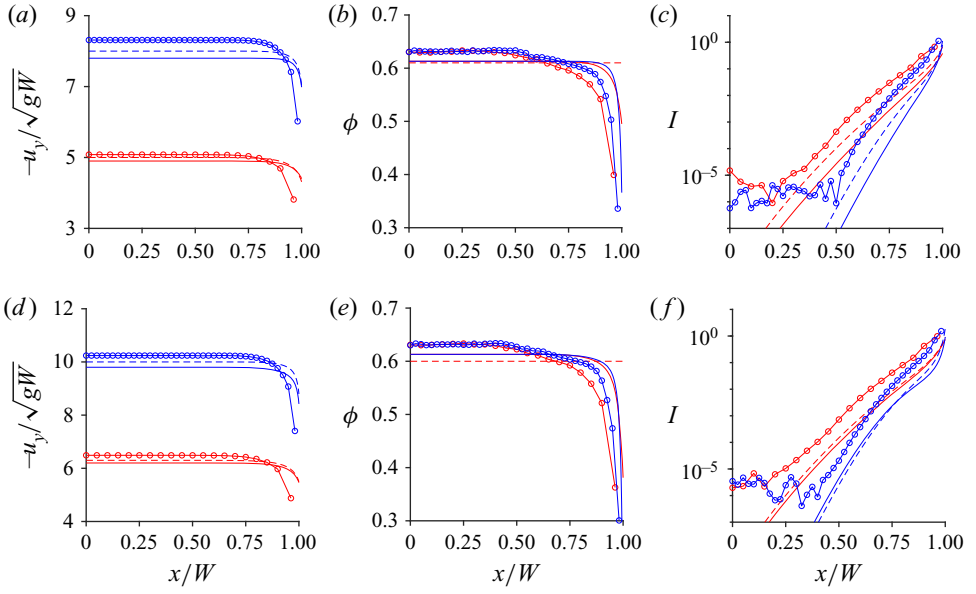

Figure 12. Variation of the scaled vertical velocity $-u_y/\sqrt{gW}$ (*a*), the solids fraction ϕ (*b*) and the inertial number I (*c*) with x/W for the model of Henann & Kamrin (2013): ○, the DEM results; blue and red dashed line, $\phi = \text{const.} = \phi_p$; blue and red solid line, $\phi = \phi(I)$; $2\,W/d_p = 40$, red curves; $2\,W/d_p = 80$, blue curves. Here, $\bar{\phi} = 0.61$ (*a–c*), and 0.60 (*d–f*).

and hence there is no obvious choice for ℓ/d_p. Clearly, ℓ should be small compared with the half-width W of the channel and large enough so that the averaging volume used to average the flow rule contains a reasonable number of particles. The smallest value of ℓ/d_p used here is 3. Choosing a value of N_{rms} that is 5 % larger than the value for $\ell/d_p = 3$, and averaging the results for $2\,W/d_p = 30$, 40 and 50, we obtain $\ell/d_p = 5$. A sphere of radius $5\,d_p$ contains ≈75 particles. The value used by Dsouza & Nott (2020) is $\ell/d_p = 10$ but the reason behind this choice is not clear. It leads to a larger discrepancy compared with the DEM results (figure 13a). As mentioned in § 3.5, the dimensionless shear rate $\tilde{S} = S'\sqrt{W/g}$ is replaced by $\tilde{S} + \tilde{\epsilon}$, where $\tilde{\epsilon}$ is chosen as 10^{-4}. The results are unaffected for $\tilde{\epsilon}$ in the range 10^{-6}–10^{-2}, and the relative error in the results with respect to $\tilde{\epsilon} = 10^{-4}$ is in the range 10^{-4} %–10^{-2} %.

The results are sensitive to the choice of the functional form of $\Pi(\phi)$, the local value of the mean stress at a critical state. The two forms used here (3.60) and (3.61) lead to very different profiles of ϕ in the shear layer and also different estimates of the normal stresses (figure 13*b*). The local contribution of the critical state pressure $\Pi(\phi)$ diverges faster for (3.61) than (3.60). The ratio of $\Pi(\phi)$ calculated from (3.61) and (3.60) for, say, $\phi(x = 0) = 0.63$ is $\approx 10^3$, which explains the much higher prediction of the scaled normal stress $\tilde{N}$ for (3.61). There is a dire need for data on $\Pi(\phi)$ at stress levels comparable to those that occur in laboratory-scale experiments.

Equation (3.64) could not be solved except for $\bar{\phi} = 0.62$. The reason for this behaviour is discussed in § 4.5.1. As the centreline velocity is forced to match the DEM value, the prediction is good near the centre (the magenta curves in figure 3*a*,*e*). However, the DEM results are significantly underestimated except close to the wall. Consequently, the predicted thickness of the shear layer is much higher (the magenta symbols in figure 4*b*). The value of l_u calculated from (3.33) varies from 1 to 20 as $2\,W/d_p$ increases from 30

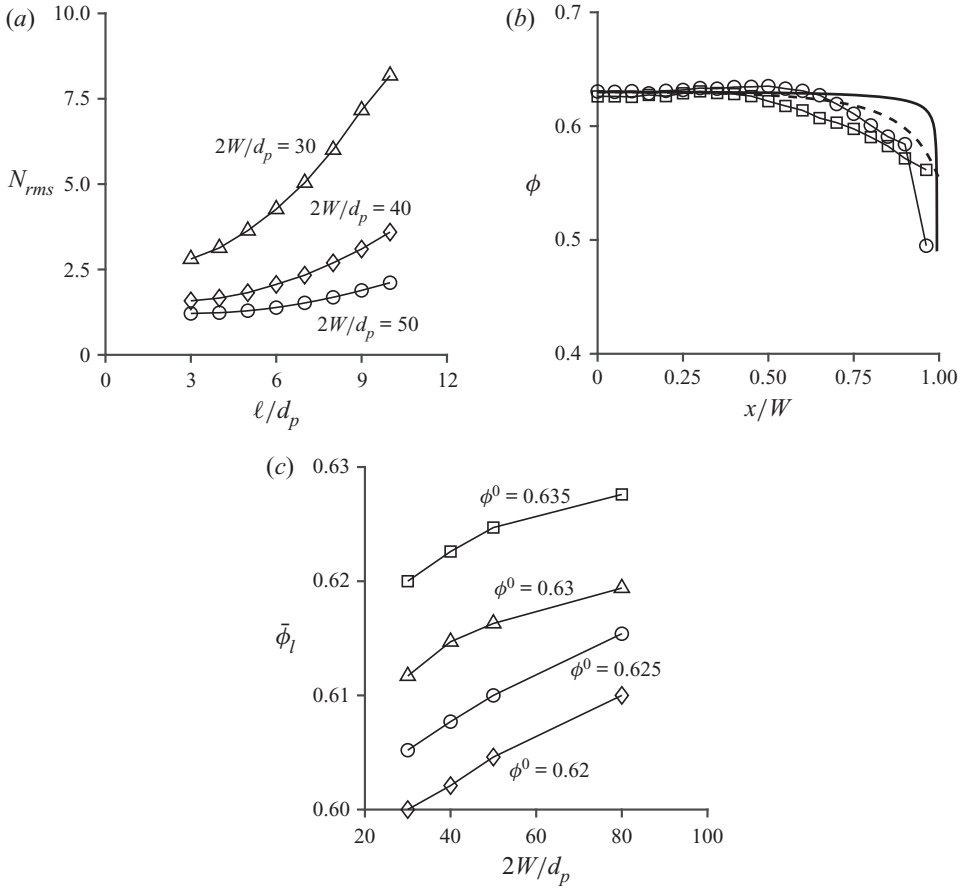

Figure 13. Variation of the root mean square error for the normal stress N_{rms} (see (4.25)) with ℓ/d_p (a), solids fraction ϕ with x/W (b) and the lower limit $\bar{\phi}_l$ for $\bar{\phi}$ with $2\,W/d_p$ and $\phi^0 \equiv \phi(x=0)$ (c) for the model of Dsouza & Nott (2020). Here, ℓ is the effective radius of averaging volume (see (3.59)). In (b), the symbols represent the DEM results for smooth (○) and rough (□) walls, and the curves represent the numerical solutions based on (3.60) (black dashed line) and (3.61) (black solid line) for $2\,W/d_p = 40$ and $\bar{\phi} = 0.62$. The scaled normal stresses $\tilde{N}$ predicted by (3.60) and (3.61) are 6.26 and 4.16×10^4 , respectively. In (c), $\bar{\phi}_l$ corresponds to $\phi(x = W) = \phi_{min}$ (see (3.60)).

to 80 (figure 4d). Hence (3.33) is not a suitable b.c. For rough walls, the magnitude of the scaled velocity changes sign near the wall, which is unrealistic. The reason for this behaviour is discussed in § 4.2.

For smooth walls, the ϕ profiles agree well with the DEM results (the magenta curves in figure 5a,e). For rough walls, discrepancies are evident for intermediate values of x/W. For a fixed value of $\bar{\phi}$, ϕ profiles depend on $\phi(x=0)$, which is matched to the DEM results. As $\phi(0)$ is found to be insensitive to the wall roughness (figure 5a,e), the predicted ϕ profiles are independent of the wall roughness, in contrast to the DEM results.

The normal stress differences are zero (the first of (3.62)). The scaled normal stress $\tilde{N}$ is much higher than the DEM results (the magenta symbols in figure 7e). The local model, obtained by setting $\ell = 0$ in (3.62)–(3.64), implies that the momentum balance (3.64) cannot be satisfied, and hence it does not predict the variation of ϕ in the current geometry. However, the local contribution to the normal stress may be readily evaluated

using the values of ϕ. For example, if $2W/d_p = 40$ and $\bar{\phi} = 0.61$, $\tilde{N}_{local}/\tilde{N} \approx 0.25$ at $x = 0$. Thus large normal stresses arise mainly from the non-local term involving ℓ^2 in the first of (3.64). As $2W/d_p$ increases, $\tilde{N}$ decreases, in contrast to the behaviour of the DEM and the other models. Some insight can be gained from an approximate solution discussed in § 4.5.2.

4.5.1. *Reasons for the lack of solutions for* $\bar{\phi} = 0.59 - 0.61$

The integration of the first of (3.64) from $x/W = 0$ stops when $\phi = \phi_{min}$ for $x/W \leqslant 1$. This is because $\Pi = 0$ for $\phi < \phi_{min}$ (see (3.60)), and hence the normal stress N vanishes (see the first of (3.64)). Thus there is a lower limit $\bar{\phi} \equiv \bar{\phi}_l$ such that $\phi(x = W) = \phi_{min}$. To obtain $\bar{\phi}_l$, we integrate the first of (3.64) using $\phi(x = 0) = \phi^0$ and $\mathrm{d}\phi/\mathrm{d}x(x = 0) = 0$, and iterate the value of N such that $\phi(x = W) = \phi_{min}$. Curves of constant ϕ^0 are shown in figure 13(*c*). For fixed values of $2W/d_p$ and ϕ^0, solutions can be obtained for $\bar{\phi} > \bar{\phi}_l$. Our DEM results predict $\phi^0 \approx 0.63$, which is one of the b.c. used to solve the first of (3.64). The curve corresponding to this value shows that solutions cannot be obtained for $\bar{\phi} \leqslant 0.61$ (figure 13*c*).

4.5.2. *Approximate solution*

The structure of (3.64) and the b.c. permits the construction of a Taylor series solution. Expanding ϕ in a Taylor series about $x = 0$, and using the symmetry condition $\mathrm{d}\phi/\mathrm{d}x(x = 0) = 0$

$$\phi = \phi^0 + \frac{1}{2}\left.\frac{\mathrm{d}^2\phi}{\mathrm{d}x^2}\right|_0 x^2 + O(x^4). \tag{4.26}$$

Using the first of (3.64)

$$\left.\frac{\mathrm{d}^2\phi}{\mathrm{d}x^2}\right|_0 = \left.\frac{\Pi - N}{\ell^2 \dfrac{\mathrm{d}\Pi}{\mathrm{d}\phi}}\right|_0. \tag{4.27}$$

Integrating (4.26) with respect to x from 0 to W, we obtain

$$\bar{\phi} = \phi^0 + \frac{1}{6}\left.\frac{\mathrm{d}^2\phi}{\mathrm{d}x^2}\right|_0 W^2. \tag{4.28}$$

Using (4.26) and (4.28), the approximate solution for ϕ is

$$\phi = \phi^0 + 3\left(\bar{\phi} - \phi^0\right)\left(\frac{x}{W}\right)^2. \tag{4.29}$$

To obtain the normal stress N, we use (4.27) and (4.28)

$$N = \Pi_{\phi=\phi^0} - 6\left(\frac{\ell}{W}\right)^2\left(\bar{\phi} - \phi^0\right)\left.\frac{\mathrm{d}\Pi}{\mathrm{d}\phi}\right|_{\phi=\phi^0}. \tag{4.30}$$

Setting $q = \mathrm{d}u_y/\mathrm{d}x$, (3.67) reduces to

$$\left.\frac{\mu_*}{q}\left(Nq - \ell^2\Pi\,\frac{\mathrm{d}^2q}{\mathrm{d}x^2}\right)\right|_x = \rho_p g\int_0^x \phi\,\mathrm{d}x'. \tag{4.31}$$

Expanding q in a Taylor series about $x = 0$, and using the conditions $q(x = 0) = 0$ and $\mathrm{d}^2q/\mathrm{d}x^2(x = 0) = 0$ (see (3.66))

$$\frac{\mathrm{d}u_y}{\mathrm{d}x} = q = \left.\frac{\mathrm{d}q}{\mathrm{d}x}\right|_0 x + \frac{1}{3!}\left.\frac{\mathrm{d}^3q}{\mathrm{d}x^3}\right|_0 x^3 + O(x^5). \tag{4.32}$$

Now, applying limit $x \to 0$ to (4.31), L'Hopital's rule implies that

$$\frac{N\left.\dfrac{\mathrm{d}q}{\mathrm{d}x}\right|_0 - \ell^2 \Pi_{\phi=\phi^0}\left.\dfrac{\mathrm{d}^3q}{\mathrm{d}x^3}\right|_0}{\left.\dfrac{\mathrm{d}q}{\mathrm{d}x}\right|_0} = 0. \tag{4.33}$$

Assuming that $\mathrm{d}q/\mathrm{d}x|_0 \neq 0$, (4.33) reduces to

$$N\left.\frac{\mathrm{d}q}{\mathrm{d}x}\right|_0 - \ell^2 \Pi_{\phi=\phi^0}\left.\frac{\mathrm{d}^3q}{\mathrm{d}x^3}\right|_0 = 0. \tag{4.34}$$

Solving for $\mathrm{d}^3q/\mathrm{d}x^3|_0$ from (4.34), integrating (4.32) and using $u_y(x = 0) \equiv u_y^0$, we obtain

$$u_y = u_y^0 + \left(\frac{1}{2}x^2 + \frac{1}{24\ell^2}\frac{N}{\Pi_{\phi=\phi^0}}x^4\right)\left.\frac{\mathrm{d}q}{\mathrm{d}x}\right|_0. \tag{4.35}$$

Using (3.32), (4.29) and (4.35), we obtain

$$\left.\frac{\mathrm{d}q}{\mathrm{d}x}\right|_0 = \frac{\left(2\rho_p B(-u_y^0)\bar{\phi}W\right) - \dot{M}}{2\rho_p B\left(\dfrac{3}{10}\bar{\phi}W^3 + \dfrac{1}{56\ell^2}\dfrac{N}{\Pi_{\phi=\phi^0}}\bar{\phi}W^5 + \dfrac{1}{60}\phi^0 W^3 - \dfrac{1}{105\ell^2}\dfrac{N}{\Pi_{\phi=\phi^0}}\phi^0 W^5\right)}. \tag{4.36}$$

The functions (4.29), (4.30), (4.35) and (4.36) provide an approximate solution. The approximate solution for the velocity is close to the numerical solution, except near the wall (figure 3*a*,*e*). Owing to the Taylor series expansion, the approximate solution can be constructed for $\bar{\phi} \leqslant 0.62$, whereas the numerical solution cannot be obtained for $\bar{\phi} < 0.62$ (see § 4.5.1). For fixed values of $\bar{\phi}$ and x/W, (4.29) shows that $\phi(x/W)$ is independent of W (the blue curves in figure 5). The numerical solution (the magenta curves in figure 5*a*,*e*) reflects this behaviour except very close to the wall. This is in keeping with the trends shown by the DEM results.

In the absence of the non-local term involving $(\ell/W)^2$ in (4.30), N is approximately a constant as ϕ^0 does not vary much with changes in $\bar{\phi}$ and $2\,W/d_p$ for the DEM results. When the non-local term is included, (4.30) shows that N increases as W decreases provided $\bar{\phi} < \phi^0$, in contrast to the DEM results (the blue symbols in figure 7*e*). The numerical solution (magenta) is close to the approximate solution. The slope $\mathrm{d}N/\mathrm{d}\bar{\phi}$ of (4.30) is negative, in contrast to the DEM results. Thus higher order terms may be required to get a more accurate solution.

5. Discussion

The problem of the gravity flow of granular material through a vertical channel is examined using the DEM and some continuum models for a wide range $2\,W/d_p = 30{-}80$

and $\bar{\phi} = 0.62{-}0.59$. In the DEM simulation, there is no exit slot in the channel, and periodic b.c.s are applied in the flow y- and the vorticity z-directions. The range of $\bar{\phi}$ appears narrow, but is not as earlier work suggests that the material does not flow for $\bar{\phi} > 0.62$. There is a lower limit $\bar{\phi} = \bar{\phi}_{cr}$ such that steady flow does not occur for $\bar{\phi} < \bar{\phi}_{cr}$. For smooth walls with $2\,W/d_p = 80$, $\bar{\phi}_{cr} = 0.59$. The value of $\bar{\phi}_{cr}$ depends on $2\,W/d_p$, and ongoing work suggests that it also depends on the wall roughness.

Let us summarize the DEM results first. They predict a plug at the centre and a shear layer near the wall, in accord with experimental observations. The solids fraction ϕ is approximately constant in the plug and reduces significantly in the shear layer because of dilation. The value of $\phi \approx 0.63$ in the plug is approximately independent of the width $2\,W/d_p$, the bulk solids fraction $\bar{\phi}$, and the wall roughness. However, in the shear layer, the profiles of ϕ vary with $\bar{\phi}$ and the wall roughness for a fixed value of $2\,W/d_p$. The scaled thickness of the shear layer Δ/d_p increases with $2\,W/d_p$, in accord with the data of Ananda *et al.* (2008). It increases as $\bar{\phi}$ decreases, and varies with the wall roughness. The mass flow rate $\dot{M}$ increases as $2\,W/d_p$ increases and $\bar{\phi}$ decreases. When $\bar{\phi}$ decreases, $-u_y$ increases more than the corresponding decrease in ϕ near the wall. Hence $\dot{M}$ increases. For smooth walls, the values of $\dot{M}$ are higher than those for rough walls, as expected. The slip length l_u/d_p is approximately independent of $2\,W/d_p$ and $\bar{\phi}$, but the values are nearly 4 times higher for smooth walls than those for rough walls. Thus it may be possible to use the slip b.c. (3.33) for solving flow problems. The inertial number I varies from very small values near the centre to large values of $O(1)$ near the wall. It increases as $\bar{\phi}$ decreases, and the values are higher near the wall for rough walls than those for smooth walls. The normal stress differences are non-zero. In granular statics, it is well known that the stress field is anisotropic (Nedderman 1992; Rao & Nott 2008). This is believed to be caused by the occurrence of stress chains, which are preferred directions along which stresses are transmitted under the influence of gravity (see e.g. Vanel *et al.* 1999). In flowing media, the shear rate may also induce anisotropy (Sun & Sundaresan 2011). None of the models examined here capture this feature. It is known that some kinetic theories predict this effect (Goldhirsch & Sela 1996; Kumaran 2006, 2008; Saha & Alam 2016; Jenkins, Alam & Berzi 2020). Some of these theories attribute the normal stress differences to the anisotropy in the second moment of the velocity fluctuations in the dilute limit, and velocity correlations arising from inelasticity in the dense limit (Saha & Alam 2016; Jenkins *et al.* 2020). The scaled normal stress $\tilde{N} = N/(\rho_p g W)$ is almost independent of $2\,W/d_p$. It increases with $\bar{\phi}$, and its values are higher for smooth walls. The angle of wall friction δ is approximately independent of $2\,W/d_p$, but it decreases as $\bar{\phi}$ increases. The value of δ is slightly higher for the rough walls. Further work is required to develop a suitable friction b.c. (3.34). Many of the results such as the profiles of ϕ (for spheres), Δ, I, l_u, δ, $\tilde{N}$ and normal stress differences have not been reported in detail earlier for the present problem.

The model of Barker *et al.* (2017) captures the trends of the velocity and normal stress qualitatively. A vertical asymptote in the I vs x profiles as $I \to 0$, and almost flat ϕ profiles are the major drawbacks. Even though $\mu(I)$ has been obtained by fitting (3.26) to the DEM data of Chialvo *et al.* (2012) in a different geometry, it does not fit our data well. Hence (3.26) is not a true constitutive equation, as mentioned earlier. The profiles of ϕ and I, and the values of Δ/d_p and $\tilde{N}$ depend on $2\,W/d_p$ and $\bar{\phi}$, but they do not vary with wall roughness. Solutions cannot be obtained for some of the parameter values used, and an approximate analysis for this behaviour has been discussed in § 4.2.1. Note that this model differs from the $\mu(I) - \phi(I)$ model as ϕ depends on I and $\tilde{N}$ (see (3.27)).

The model of Schaeffer *et al.* (2019) reduces to the $\mu(I) - \phi(I)$ model only for the case of steady, fully developed flow. It is easier to use than the model of Barker *et al.* (2017). An analytical solution for I has been obtained based on the assumed linear relation between ϕ and I. The ϕ profiles agree much better with the DEM results than the model of Barker *et al.* (2017). As the form of $\mu(I)$ is the same for both the models, the undesirable feature of the I vs x profiles persists. There is not much improvement in the prediction of the velocity and the normal stress. Similar to Barker *et al.* (2017), the predictions of ϕ, I and $\tilde{N}$ are independent of wall roughness. Because of the functional form assumed for $\phi(I)$, the profiles of I vs x/W, ϕ vs x/W and $\tilde{N}$ vs. $\bar{\phi}$ are independent of $2\,W/d_p$, unlike the model of Barker *et al.* (2017). However, the linear function of $\phi(I)$ may not hold for much lower and higher values of I (Chialvo *et al.* 2012). Our DEM data for ϕ vs I also show a more complex behaviour.

The non-local model of Henann & Kamrin (2013) introduces a new variable called the fluidity f, and the governing equation for f incorporates the higher gradient of shear rate. It predicts the velocity and I profiles fairly well, but fails to account for the variation in ϕ near the wall, as ϕ is assumed to be a constant. Henann & Kamrin (2013) found an excellent agreement between their velocity profiles at the free surface of a split-bottom Couette cell and measurements. Thus it is important to test constitutive equations in various geometries and examine profiles of several variables. Because ϕ is treated as a constant, $\tilde{N}$ is indeterminate. Hence we have matched $\tilde{N}$ to the DEM results, in contrast to the other models. For some values of parameters, the model predicts negative values of f, which is unrealistic. Some insight into this behaviour is provided by the analysis discussed in § 4.4.2. The assumption that $\phi = \phi(I)$ leads to more realistic ϕ profiles.

Dsouza & Nott (2020) obtain the value of ϕ at a point by averaging its local value, which is assumed to depend on the mean stress at a critical state, over a representative volume. In the present problem, this causes the ϕ profiles to be independent of the shear rate, unlike the $\mu(I) - \phi(I)$ model. It is supposed to be valid only in the limit $I \to 0$, but it has been used here even though I is of $O(1)$ near the wall. The trends of the velocity and ϕ are predicted reasonably well, but $\tilde{N}$ is much higher than the DEM results. It predicts a thin plug zone, in contrast to the DEM results and the other models. The model could be solved only for $\bar{\phi} = 0.62$, for reasons explained in § 4.5.1. For smaller values of $\bar{\phi}$, ϕ attains a value ϕ_{min} at some value of x, and hence $\tilde{N} = 0$. An approximate solution obtained by a Taylor series expansion agrees reasonably well with the numerical solution. Though the non-local terms are supposed to be small in magnitude compared with the local terms, this is not true in the present problem, in contrast to the underlying assumption that they represent small corrections. Either the inclusion of higher-order terms or terms involving rate-dependent effects may remedy the situation. This may be a fertile area for research. However, this poses serious problems with the regard to the specification of suitable b.c.s.

As the inertial number I varies from zero at the centre to large values at the wall, none of the four continuum models examined here agree well with the DEM results. Some predict the velocity profiles reasonably well but not the solids fraction profiles, even after matching the bulk solids fraction and the mass flow rate with the DEM results. The converse is true for the other models. The models examined here are loosely based on extensions of the equations for slow, rate-independent flow. It appears that a model which includes collisional effects more explicitly, such as kinetic theory, should be combined in some manner with the present models to obtain more realistic models.

For smooth walls, the DEM results show sharp changes near the wall for many of the variables such as the velocity and the solids fraction. Perhaps continuum models are not

applicable in the region very close to the wall. Hence this may motivate researchers to develop suitable models for the wall region.

Except for the model of Henann & Kamrin (2013), the slip length l_u (see (3.33)) depends on $\bar{\phi}$ and $2\,W/d_p$, and hence is not a material parameter. The angle of wall friction δ (see (3.35)) depends on $\bar{\phi}$ and $2\,W/d_p$, except the model of Schaeffer *et al.* (2019) where it depends on $\bar{\phi}$. On the other hand, the DEM results suggest that l_u depends only on the wall roughness, and δ depends on both the wall roughness and $\bar{\phi}$. Further effort is needed to develop suitable b.c. for all the models. As N. R. Amundson used to say, 'Boundary conditions must come from nature'. We must turn to experiments, micromechanical models, and simulations in our quest for b.c.s.

The contact forces in the DEM involve a spring (elastic effects), a dashpot (viscous or rate-dependent effects) and a slider (frictional or rate-independent effects). None of the models used in the present work involve elastic effects. The models of Berzi & Jenkins (2015) and Berzi, Jenkins & Richard (2020) explicitly include the stiffness k_n in the constitutive equations based on kinetic theory to allow for the non-zero duration of particle interactions. In the paper of Berzi *et al.* (2020), k_n has been included even though $p\,d_p/k_n \approx 7 \times 10^{-5}$ at the base of an inclined chute. However, the results have not been compared with the case $k_n \to \infty$. Berzi & Jenkins (2015) show that the results obtained for a range of k_n values (typically used in DEM simulations) differ from those for the rigid particle limit. A preliminary analysis of a difficulty encountered in using the model of Berzi *et al.* (2020) is given in Appendix A.

Acknowledgements. We are grateful to the Supercomputer Education and Research Centre (SERC), IISc for providing computational support, the referees for their very helpful comments in earlier version of the manuscript and T. Barker, D. Berzi, D.L. Henann, K. Kamrin, P.R. Nott and O. Pouliquen for helpful discussions.

Funding. This work was supported by funding from the MHRD and the Science and Engineering Research Board, Government of India (Grant no. CRG/2018/002673 and SR/S2/JCB-31/2006).

Declaration of interests. The authors report no conflict of interest.

Author ORCIDs.
Bhanjan Debnath https://orcid.org/0000-0002-3734-8823;
V. Kumaran https://orcid.org/0000-0001-9793-6523;
K. Kesava Rao https://orcid.org/0000-0002-8890-7904.

Author contributions. B.D. and K.K.R. formulated the problem statement, analysis and conclusions and V.K. provided suggestions on improving models and formulating boundary conditions.

Appendix A. Remarks on the extended kinetic theory of Berzi *et al.* (2020)

The model has two sets of constitutive equations, set S_1 for $\phi > \phi_i$, and set S_2 for $\phi < \phi_i$. Based on the work of Chialvo *et al.* (2012), Berzi *et al.* (2020) used $\phi_i = 0.587$. In the present problem, (3.7*a*,*b*) and (3.21*a*,*b*) have to be solved along with the pseudo-thermal energy balance

$$\tau \frac{\mathrm{d}u_y}{\mathrm{d}x} = \frac{\mathrm{d}Q}{\mathrm{d}x} + \Gamma. \tag{A1}$$

Omitting the adjective 'pseudo-thermal' for brevity, Q and Γ are the heat flux and the rate of dissipation of energy per unit volume due to collisions, respectively. Let x_i be defined by $\phi(x_i) = \phi_i$. Consider an interface at $x = x_i$ where $\phi = \phi_i$. It is assumed that the velocity u_y, the solids fraction ϕ and the granular temperature T, which is a measure of velocity

$$f_1 = \phi(1 + 2G(1 + e_n))$$

$$f_c = \left[1 + \frac{12}{5} G \frac{T_*^{1/2}}{k_{n*}^{1/2}}\right]^{-1}$$

$$G = \phi f_\phi$$

$$\text{for } 0.4 \leqslant \phi < \phi_i, f_\phi = \left[1 - \left(\frac{\phi - 0.4}{\phi_i - 0.4}\right)^2\right] \frac{2 - \phi}{2(1 - \phi)^3} + \left(\frac{\phi - 0.4}{\phi_i - 0.4}\right)^2 \frac{2}{\phi_i - \phi}$$

$$\text{for } \phi < 0.4, f_\phi = \frac{2 - \phi}{2(1 - \phi)^3}$$

$$f_4 = \frac{4M\phi G}{\pi^{1/2}}$$

$$f_5 = \frac{25\pi^{1/2} V}{128\phi}$$

$$M = \frac{1 + e_n}{2} + \frac{9\pi}{144(1 + e_n)G^2} \frac{[5 + 3G(2e_n - 1)(1 + e_n)^2][5 + 6G(1 + e_n)]}{16 - 7(1 - e_n)}$$

$$\text{as } \phi \to \phi_i, M \to M_\infty = \frac{1 + e_n}{2} + \frac{9\pi}{8(1 + e_n)} \frac{(2e_n - 1)(1 + e_n)^3}{16 - 7(1 - e_n)}$$

$$V = \frac{96\phi(1 - e_n)}{25G(1 + e_n)} \frac{5 + 6G(1 + e_n)}{16 + 3(1 - e_n)} \left[\frac{20[5 + 3G(2e_n - 1)(1 + e_n)^2]}{48 - 21(1 - e_n)} \frac{\phi}{G} \frac{\mathrm{d}G}{\mathrm{d}\phi} - (e_n + e_n^2)\left(G + \phi \frac{\mathrm{d}G}{\mathrm{d}\phi}\right)\right]$$

$$J_\infty = \frac{1 + e_n}{2} + \frac{\pi}{4} \frac{(1 + e_n)^2(3e_n - 1)}{[24 - 6(1 - e_n)^2 - 5(1 - e_n^2)]}$$

$$L_c = 1 + \frac{26(1 - e_{eff})}{15} \frac{\phi_i - 0.49}{0.64 - \phi_i}$$

Table 2. Functions used in Berzi *et al.* (2020).

fluctuations, are continuous at $x = x_i$. The normal stress N, the shear stress τ and the heat flux Q must be continuous at $x = x_i$. It can be shown that N and τ are continuous, and the latter implies that the shear rate is continuous. The condition for the continuity of Q is discussed below.

Scaling the distance x, velocity u_y, temperature T, spring stiffness k_n, stresses (N, τ) and heat flux Q by d_p, $\sqrt{gd_p}$, gd_p, $\rho_p g d_p^2$, $\rho_p g d_p$ and $\rho_p (gd_p)^{3/2}$, respectively, and using $*$ to denote dimensionless variables, the constitutive equations for the heat flux Q_* are given by

$$Q_* = -f_c f_4 T_*^{1/2} \frac{\mathrm{d}T_*}{\mathrm{d}x_*} - f_c f_5 T_*^{3/2} \frac{\mathrm{d}\phi}{\mathrm{d}x_*} \quad \text{for } \phi < \phi_i \tag{A2}$$

$$Q_* = -\frac{5M_\infty \phi}{3\pi^{1/2}} k_{n*}^{1/2} \frac{\mathrm{d}T_*}{\mathrm{d}x_*} \quad \text{for } \phi > \phi_i, \tag{A3}$$

where f_c, f_4, f_5 and M_∞ are given in table 2. Here, k_{n*} and e_n are the scaled spring stiffness and the coefficient of restitution in the normal direction, respectively. Berzi *et al.* (2020) have neglected the term involving $\mathrm{d}\phi/\mathrm{d}x_*$ in (A3). They state that inclusion of this term does not significantly affect their results for chute flow. However, this may not be true in other problems.

Equation (A2) may be rewritten as

$$Q_* = b_1 + b_2 \tag{A4}$$

where

$$b_1 = -f_c f_4 T_*^{1/2} \frac{\mathrm{d}T_*}{\mathrm{d}x_*}; \quad b_2 = -f_c f_5 T_*^{3/2} \frac{\mathrm{d}\phi}{\mathrm{d}x_*}. \tag{A5a,b}$$

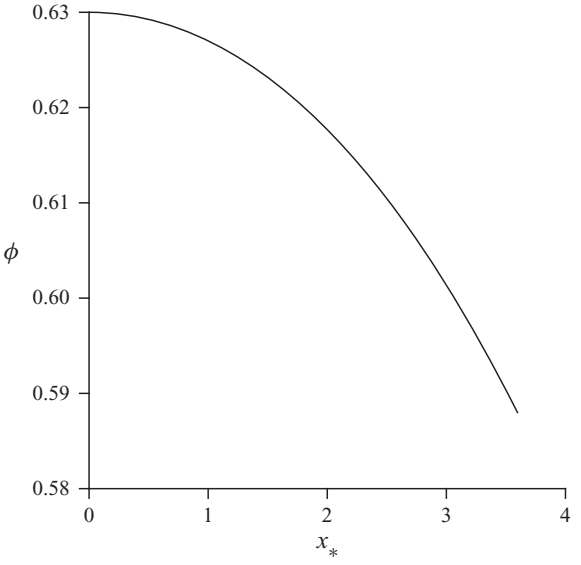

Figure 14. Variation of ϕ with $x_* = x/d_p$ using the constitutive equations of Berzi *et al.* (2020) in the region $0 \leqslant x_* \leqslant x_{*i}$, where $\phi(x_* = x_{*i}) = \phi_i = 0.587$. Parameter values: $2\,W/d_p = 50$, $\bar{\phi} = 0.61$, $\phi(x_* = 0) = 0.63$, $N_* = 42$, $u_{y*}(x_* = 0) = -26$, $e_n = 0.7$ and $k_{n*} = 10^6$.

The equation for N_* for $\phi > \phi_i$ is given by (Berzi *et al.* 2020)

$$N_* = \tfrac{5}{6}(1 + e_n)k_{n*}^{1/2}T_*^{1/2} + 0.0006(\phi - \phi_i)k_{n*}. \tag{A6}$$

Considering the limit $\phi \to \phi_i^+$

$$N_* \to \tfrac{5}{6}(1 + e_n)k_{n*}^{1/2}T_*^{1/2}. \tag{A7}$$

Hence T_* must be non-zero in this limit as $N_* > 0$ and the quantity $GT_*^{1/2}$ in the expression for $f_c \to \infty$ (see table 2). Then

$$b_1 \to -\frac{5}{3\pi^{1/2}}\,k_{n*}^{1/2}M_\infty\phi_i\,\frac{\mathrm{d}T_*}{\mathrm{d}x_*} \quad \text{as } \phi \to \phi_i^-. \tag{A8}$$

The right-hand side of (A8) is identical to the expression for Q_* at $\phi = \phi_i^+$ (see (A3)), provided the slope of T_* is continuous at x_*.

As $\phi \to \phi_i^-, f_c \propto (\phi_i - \phi)$, and $V \propto (\phi_i - \phi)^{-2}$ (see table 2). Hence $|f_c f_5| \to \infty$ in this limit. It is reasonable to expect that the heat flux Q_* is bounded at $x_* = x_{*i}$, or equivalently, $\phi = \phi_i$. This requirement and the non-zero value of $T_*(x_*)$, together with (A4) implies that

$$\frac{\mathrm{d}\phi}{\mathrm{d}x_*} \to 0 \quad \text{as } \phi \to \phi_i^-. \tag{A9}$$

It is not clear that the slope of ϕ is continuous at $x_* = x_{*i}$. To understand this behaviour, a preliminary attempt to solve the equations (set S_1) for $0 \leqslant x_* < x_{*i}$ is described below.

Set S_1 consists of (A3) for Q_*, (A6) for N_*, (A10) for τ_* and (A11) for Γ, where

$$\tau_* = b_3 \frac{N_*}{T_*^{1/2}} \frac{\mathrm{d}u_{y*}}{\mathrm{d}x_*} \quad \text{for } \phi > \phi_i \tag{A10}$$

$$\Gamma = \frac{5(1-e_{eff}^2)\phi}{\sqrt{\pi} L_c} k_{n*}^{1/2} T_*. \tag{A11}$$

Here, $b_3 = (4J_\infty)/(5\pi^{1/2}(1+e_n))$, $e_{eff} = 0.645$ and J_∞ and L_c are given in table 2. Using (3.21*a*,*b*), (A3), (A6) and (A10), the balance equations (3.7*a*,*b*) and (A1) are integrated from $x_* = 0$ to $x_* = x_{*i}$, where $\phi = \phi_i$. Three conditions, namely, $\phi(x_* = 0)$, N_* and $u_{y*}(x_* = 0)$ are taken from the DEM results, and $T_*(x_* = 0)$ is calculated from (A6). In addition, the symmetry conditions $\tau_*(x_* = 0) = 0$ and $Q_*(x_* = 0) = 0$ are used. For $2W/d_p = 50$ and $\bar{\phi} = 0.61$, the ϕ profile shows that $\mathrm{d}\phi/\mathrm{d}x_* < 0$ as $x_* \to x_{*i}^-$ (figure 14). As $\mathrm{d}\phi/\mathrm{d}x_* \to 0$ as $x_* \to x_{*i}^+$, the slope of the ϕ profile is discontinuous at $x_* = x_{*i}$, in contrast to the DEM results (figure 5). As noted by one of the referees, there is no physical requirement for the slopes of the T_* and ϕ profiles to be continuous at x_*. If the DEM results are accepted as a reasonable description of reality, then the model shows an undesirable feature at the interface. More work is needed to decide whether the constitutive equations for the model, or the DEM or both, should be modified. As R. von Mises said, 'The leitmotif, the ever-recurring melody, is that two things are essential in any description of a segment of reality: to submit to experience and face the language used with unceasing logical criticism'.

References

Allen, M.P. & Tildesley, D.J. 2017 *Computer Simulation of Liquids*. Oxford University Press.

Ananda, K.S., Moka, S. & Nott, P.R. 2008 Kinematics and statistics of dense, slow granular flow through vertical channels. *J. Fluid Mech.* **610**, 69–97.

Aranson, I.S. & Tsimring, L.S. 2001 Continuum description of avalanches in granular media. *Phys. Rev.* E **64**, 020301.

Barker, T. & Gray, J.M.N.T. 2017 Partial regularisation of the incompressible $\mu(I)$-rheology for granular flow. *J. Fluid Mech.* **828**, 5–32.

Barker, T., Schaeffer, D.G., Bohórquez, P. & Gray, J.M.N.T. 2015 Well-posed and ill-posed behaviour of the $\mu(I)$-rheology for granular flow. *J. Fluid Mech.* **779**, 794–818.

Barker, T., Schaeffer, D.G., Shearer, M. & Gray, J.M.N.T. 2017 Well-posed continuum equations for granular flow with compressibility and $\mu(I)$-rheology. *Proc. R. Soc. Lond.* A **473**, 20160846.

Batchelor, G.K. 1967 *An Introduction to Fluid Dynamics*. Cambridge University Press.

Berryman, J.G. 1983 Random close packing of hard spheres and disks. *Phys. Rev.* A **27**, 1053.

Berzi, D. & Jenkins, J.T. 2015 Steady shearing flows of deformable, inelastic spheres. *Soft Matt.* **11**, 4799–4808.

Berzi, D., Jenkins, J.T. & Richard, P. 2020 Extended kinetic theory for granular flow over and within an inclined erodible bed. *J. Fluid Mech.* **885**, A27.

Beverloo, W.A., Leniger, H.A. & Van de Velde, J. 1961 The flow of granular solids through orifices. *Chem. Engng Sci.* **15**, 260–269.

Bharathraj, S. & Kumaran, V. 2017 Effect of base topography on dynamics and transition in a dense granular flow. *J. Fluid Mech.* **832**, 600–640.

Bharathraj, S. & Kumaran, V. 2019 Cessation of a dense granular flow down an inclined plane. *Phys. Rev. Fluids* **4** (2), 024301.

Bhateja, A. & Khakhar, D.V. 2020 Analysis of granular rheology in a quasi-two-dimensional slow flow by means of discrete element method based simulations. *Phys. Fluids* **32**, 013301.

Bouzid, M., Izzet, A., Trulsson, M., Clément, E., Claudin, P. & Andreotti, B. 2015 Non-local rheology in dense granular flows. *Eur. Phys. J.* E **38**, 125.

BRENNEN, C. & PEARCE, J.C. 1978 Granular material flow in two-dimensional hoppers. *J. Appl. Mech.* **45**, 43–50.

CHIALVO, S., SUN, J. & SUNDARESAN, S. 2012 Bridging the rheology of granular flows in three regimes. *Phys. Rev.* E **85**, 021305.

CUNDALL, P.A. & STRACK, O.D.L. 1979 A discrete numerical model for granular assemblies. *Gèotechnique* **29**, 47–65.

DA CRUZ, F., EMAM, S., PROCHNOW, M., ROUX, J. & CHEVOIR, F. 2005 Rheophysics of dense granular materials: discrete simulation of plane shear flows. *Phys. Rev.* E **72**, 021309.

DANCZYK, M., MEACLEM, T., MEHDIZAD, M., CLARKE, D., GALVOSAS, P., FULLARD, L. & HOLLAND, D. 2020 Influence of contact parameters on discrete element method (DEM) simulations of flow from a hopper: comparison with magnetic resonance imaging (MRI) measurements. *Powder Technol.* **372**, 671–684.

DEBNATH, B., KUMARAN, V. & RAO, K.K. 2019 The transition from steady non-oscillatory flow to oscillatory flow of granular material through a vertical channel: a DEM study. Paper presented at the *2019 AIChE Annual Meeting, Orlando*.

DEBNATH, B., RAO, K.K. & NOTT, P.R. 2017 The lift on a disc immersed in a rotating granular bed. *AIChE J.* **63**, 5482–5489.

DI RENZO, A. & DI MAIO, F.P. 2004 Comparison of contact-force models for the simulation of collisions in DEM-based granular flow codes. *Chem. Engng Sci.* **59**, 525–541.

DSOUZA, P.V. & NOTT, P.R. 2020 A non-local constitutive model for slow granular flow that incorporates dilatancy. *J. Fluid Mech.* **888**, R3.

FENISTEIN, D. & VAN HECKE, M. 2003 Wide shear zones in granular bulk flow. *Nature* **425**, 256–256.

FICKIE, K.E., MEHRABI, R. & JACKSON, R. 1989 Density variations in a granular material flowing from a wedge-shaped hopper. *AIChE J.* **35**, 853–855.

FORTERRE, Y. & POULIQUEN, O. 2003 Long-surface-wave instability in dense granular flows. *J. Fluid Mech.* **486**, 21–50.

GARZÓ, V. & DUFTY, J.W. 1999 Dense fluid transport for inelastic hard spheres. *Phys. Rev.* E **59**, 5895.

GDR-MIDI 2004 On dense granular flows. *Eur. Phys. J.* E **14**, 341–365.

GODDARD, J.D. & LEE, J. 2017 On the stability of the $\mu(I)$ rheology for granular flow. *J. Fluid Mech.* **833**, 302–331.

GODDARD, J.D. & LEE, J. 2018 Regularization by compressibility of the $\mu(I)$ model of dense granular flow. *Phys. Fluids* **30**, 073302.

GOLDHIRSCH, I. & SELA, N. 1996 Origin of normal stress differences in rapid granular flows. *Phys. Rev.* E **54**, 4458–4461.

GONZÁLEZ-MONTELLANO, C., AYUGA, F. & OOI, J.Y. 2011 Discrete element modelling of grain flow in a planar silo: influence of simulation parameters. *Granul. Matt.* **13**, 149–158.

GOODMAN, M.A. & COWIN, S.C. 1971 Two problems in the gravity flow of granular materials. *J. Fluid Mech.* **45**, 321–339.

GUO, Y. & CURTIS, J.S. 2015 Discrete element method simulations for complex granular flows. *Annu. Rev. Fluid Mech.* **47**, 21–46.

HENANN, D.L. & KAMRIN, K. 2013 A predictive, size-dependent continuum model for dense granular flows. *Proc. Natl Acad. Sci. USA* **110**, 6730–6735.

HERTZ, H. 1882 Uber die beruhrung fester elastische korper and uber die harte (On the contact of elastic solids). *J. Reine Angew. Math.* **92**, 156–171.

HEYMAN, J., DELANNAY, R., TABUTEAU, H. & VALANCE, A. 2017 Compressibility regularizes the $\mu(I)$-rheology for dense granular flows. *J. Fluid Mech.* **830**, 553–568.

HOOVER, W.G. & REE, F.H. 1968 Melting transition and communal entropy for hard spheres. *J. Chem. Phys.* **49**, 3609–3617.

JACKSON, R. 1983 Some mathematical and physical aspects of continuum models for the motion of granular materials. In *Theory of Dispersed Multiphase Flow* (ed. R.E. Meyer), pp. 291–337. Academic.

JENKINS, J.T., ALAM, M. & BERZI, D. 2020 Singular behavior of the stresses in the limit of random close packing in collisional, simple shearing flows of frictionless spheres. *Phys. Rev. Fluids* **5**, 072301.

JOHNSON, K.L. 1987 *Contact Mechanics*. Cambridge University Press.

JOHNSON, P.C., NOTT, P. & JACKSON, R. 1990 Frictional–collisional equations of motion for participate flows and their application to chutes. *J. Fluid Mech.* **210**, 501–535.

JOP, P., FORTERRE, Y. & POULIQUEN, O. 2005 Crucial role of sidewalls in granular surface flows: consequences for the rheology. *J. Fluid Mech.* **541**, 167–192.

JOP, P., FORTERRE, Y. & POULIQUEN, O. 2006 A constitutive law for dense granular flows. *Nature* **441**, 727–730.

JYOTSNA, R. & RAO, K.K. 1997 A frictional–kinetic model for the flow of granular materials through a wedge-shaped hopper. *J. Fluid Mech.* **346**, 239–270.

KAMRIN, K. & HENANN, D.L. 2015 Nonlocal modeling of granular flows down inclines. *Soft Matt.* **11**, 179–185.

KAMRIN, K. & KOVAL, G. 2012 Nonlocal constitutive relation for steady granular flow. *Phys. Rev. Lett.* **108**, 178301.

KRUGGEL-EMDEN, H., SIMSEK, E., RICKELT, S., WIRTZ, S. & SCHERER, V. 2007 Review and extension of normal force models for the discrete element method. *Powder Technol.* **171**, 157–173.

KUMARAN, V. 1998 Kinetic theory for a vibro-fluidized bed. *J. Fluid Mech.* **364**, 163–185.

KUMARAN, V. 2006 The constitutive relation for the granular flow of rough particles, and its application to the flow down an inclined plane. *J. Fluid Mech.* **561**, 1–42.

KUMARAN, V. 2008 Dense granular flow down an inclined plane: from kinetic theory to granular dynamics. *J. Fluid Mech.* **599**, 121–168.

LI, S. & HENANN, D.L. 2019 Material stability and instability in non-local continuum models for dense granular materials. *J. Fluid Mech.* **871**, 799–830.

LUN, C.K.K., SAVAGE, S.B., JEFFREY, D.J. & CHEPURNIY, N. 1984 Kinetic theories for granular flow: inelastic particles in Couette flow and slightly inelastic particles in a general flowfield. *J. Fluid Mech.* **140**, 223–256.

LUO, K., WANG, S., YANG, S., HU, C. & FAN, J. 2017 Computational fluid dynamics–discrete element method investigation of pressure signals and solid back-mixing in a full-loop circulating fluidized bed. *Ind. Engng Chem. Res.* **56**, 799–813.

MISHRA, B.K. & MURTY, C.V.R. 2001 On the determination of contact parameters for realistic DEM simulations of ball mills. *Powder Technol.* **115**, 290–297.

MOHAN, L.S., NOTT, P.R. & RAO, K.K. 1997 Fully developed flow of coarse granular materials through a vertical channel. *Chem. Engng Sci.* **52**, 913–933.

MOHAN, L.S., NOTT, P.R. & RAO, K.K. 1999 A frictional Cosserat model for the flow of granular materials through a vertical channel. *Acta Mechanica* **138**, 75–96.

MOHAN, L.S., RAO, K.K. & NOTT, P.R. 2002 A frictional Cosserat model for the slow shearing of granular materials. *J. Fluid Mech.* **457**, 377–409.

MÜHLHAUS, H. & VARDOULAKIS, I. 1987 The thickness of shear bands in granular materials. *Gèotechnique* **37**, 271–283.

NATARAJAN, V.V.R., HUNT, M.L. & TAYLOR, E.D. 1995 Local measurements of velocity fluctuations and diffusion coefficients for a granular material flow. *J. Fluid Mech.* **304**, 1–25.

NEDDERMAN, R.M. 1992 *Statics and Kinematics of Granular Materials*. Cambridge University Press.

NEDDERMAN, R.M. & LAOHAKUL, C. 1980 The thickness of the shear zone of flowing granular materials. *Powder Technol.* **25**, 91–100.

NEDDERMAN, R.M., TÜZÜN, U., SAVAGE, S.B. & HOULSBY, G.T. 1982 The flow of granular materials—I: discharge rates from hoppers. *Chem. Engng Sci.* **37**, 1597–1609.

PITMAN, E.B. & SCHAEFFER, D.G. 1987 Stability of time dependent compressible granular flow in two dimensions. *Commun. Pure Appl. Maths* **40**, 421–447.

PLIMPTON, S. 1995 Fast parallel algorithms for short-range molecular dynamics. *J. Comput. Phys.* **117**, 1–19.

POULIQUEN, O. 1999 Scaling laws in granular flows down rough inclined planes. *Phys. Fluids* **11**, 542–548.

POULIQUEN, O., CASSAR, C., JOP, P., FORTERRE, Y. & NICOLAS, M. 2006 Flow of dense granular material: towards simple constitutive laws. *J. Stat. Mech.* **2006**, P07020.

POULIQUEN, O. & FORTERRE, Y. 2002 Friction law for dense granular flows: application to the motion of a mass down a rough inclined plane. *J. Fluid Mech.* **453**, 133–151.

POULIQUEN, O. & FORTERRE, Y. 2009 A non-local rheology for dense granular flows. *Phil. Trans. R. Soc. Lond.* A **367**, 5091–5107.

POULIQUEN, O., FORTERRE, Y. & LE DIZES, S. 2001 Slow dense granular flows as a self-induced process. *Adv. Complex Syst.* **4**, 441–450.

POULIQUEN, O. & GUTFRAIND, R. 1996 Stress fluctuations and shear zones in quasistatic granular chute flows. *Phys. Rev.* E **53**, 552–561.

PRAKASH, J.R. & RAO, K.K. 1988 Steady compressible flow of granular materials through a wedge-shaped hopper: the smooth wall, radial gravity problem. *Chem. Engng Sci.* **43**, 479–494.

RAO, K.K. & NOTT, P.R. 2008 *An Introduction to Granular Flow*. Cambridge University Press.

REYNOLDS, O. 1885 On the dilatancy of media composed of rigid particles in contact. With experimental illustrations. *Phil. Mag.* **20**, 469–481.

SAHA, S. & ALAM, M. 2016 Normal stress differences, their origin and constitutive relations for a sheared granular fluid. *J. Fluid Mech.* **795**, 549–580.

SAVAGE, S.B. 1979 Gravity flow of cohesionless granular materials in chutes and channels. *J. Fluid Mech.* **92**, 53–96.

SAVAGE, S.B. & SAYED, M. 1979 Gravity flow of cohesionless granular materials in wedge-shaped hoppers. In *Mechanics Applied to the Transport of Bulk Materials* (ed. S.C. Cowin), pp. 1–24. ASME.

SCHAEFFER, D.G. 1987 Instability in the evolution equations describing incompressible granular flow. *J. Differ. Equ.* **66**, 19–50.

SCHAEFFER, D.G., BARKER, T., TSUJI, D., GREMAUD, P., SHEARER, M. & GRAY, J.M.N.T. 2019 Constitutive relations for compressible granular flow in the inertial regime. *J. Fluid Mech.* **874**, 926–951.

SCHOFIELD, A.N. & WROTH, P. 1968 *Critical State Soil Mechanics*. McGraw-Hill.

SCOTT, G.D. 1960 Packing of spheres: packing of equal spheres. *Nature* **188**, 908–909.

SCOTT, G.D. & KILGOUR, D.M. 1969 The density of random close packing of spheres. *J. Phys.* D*: Appl. Phys.* **2**, 863–866.

SHÄFER, J., DIPPEL, S. & WOLF, D.E. 1996 Force schemes in simulations of granular materials. *J. Phys. (Paris)* **6**, 5–20.

SILBERT, L.E., ERTAŞ, D., GREST, G.S., HALSEY, T.C., LEVINE, D. & PLIMPTON, S.J. 2001 Granular flow down an inclined plane: Bagnold scaling and rheology. *Phys. Rev.* E **64**, 051302.

SOKOLOVSKII, V.V. 1965 *Statics of Granular Media*. Pergamon.

SRIVASTAVA, A. & SUNDARESAN, S. 2003 Analysis of a frictional–kinetic model for gas–particle flow. *Powder Technol.* **129**, 72–85.

SUN, J. & SUNDARESAN, S. 2011 A constitutive model with microstructure evolution for flow of rate-independent granular materials. *J. Fluid Mech.* **682**, 590–616.

TEJCHMAN, J. & GUDEHUS, G. 1993 Silo-music and silo-quake experiments and a numerical Cosserat approach. *Powder Technol.* **76**, 201–212.

TEJCHMAN, J. & WU, W. 1993 Numerical study on patterning of shear bands in a Cosserat continuum. *Acta Mechanica* **99**, 61–74.

VANEL, L., HOWELL, D., CLARK, D., BEHRINGER, R.P. & CLÉMENT, E. 1999 Memories in sand: experimental tests of construction history on stress distributions under sandpiles. *Phys. Rev.* E **60**, R5040.

VU-QUOC, L., ZHANG, X. & LESBURG, L. 2001 Normal and tangential force–displacement relations for frictional elasto-plastic contact of spheres. *Intl J. Solids Struct.* **38**, 6455–6489.

WANG, C.H., JACKSON, R. & SUNDARESAN, S. 1997 Instabilities of fully developed rapid flow of a granular material in a channel. *J. Fluid Mech.* **342**, 179–197.

WÓJCIK, M. & TEJCHMAN, J. 2009 Modeling of shear localization during confined granular flow in silos within non-local hypoplasticity. *Powder Technol.* **192**, 298–310.

YALAMANCHILI, R.C., GUDHE, R. & RAJAGOPAL, K.R. 1994 Flow of granular materials in a vertical channel under the action of gravity. *Powder Technol.* **81**, 65–73.

YU, Y. & SAXÉN, H. 2010 Experimental and DEM study of segregation of ternary size particles in a blast furnace top bunker model. *Chem. Engng Sci.* **65**, 5237–5250.

ZAITSEV, V.F. & POLYANIN, A.D. 2002 *Handbook of Exact Solutions for Ordinary Differential Equations*. CRC.

ZHANG, Q. & KAMRIN, K. 2017 Microscopic description of the granular fluidity field in nonlocal flow modeling. *Phys. Rev. Lett.* **118**, 058001.

ZHAO, YA., YANG, S., ZHANG, L. & CHEW, J.W. 2018 DEM study on the discharge characteristics of lognormal particle size distributions from a conical hopper. *AIChE J.* **64**, 1174–1190.